THE ASTROPHYSICAL JOURNAL, 349:168–189, 1990 January 20

WINDS FROM T TAURI STARS. I. SPHERICALLY SYMMETRIC MODELS

LEE HARTMANN,[1] NURIA CALVET,[2,3] EUGENE H. AVRETT,[1] AND RUDOLF LOESER[1]

Received 1989 March 16; accepted 1989 July 14

ABSTRACT

As a first step toward understanding the origin of T Tauri winds, we compute emission fluxes and profiles for lines of hydrogen, Mg II, Ca II, and Na I for a sequence of spherically symmetric wind models. Our calculations indicate that the Hα emission of T Tauri stars arises in an extended and probably turbulent circumstellar envelope at temperatures $\gtrsim 8000$ K. Spherical wind models with temperatures $\lesssim 10{,}000$ K tend to produce Balmer line profiles with much deeper absorption reversals than observed. The models predict that Mg II resonance line emission should be strongly correlated with Hα fluxes; observed Mg II/Hα ratios are inconsistent with the models unless extinction corrections have been underestimated. The models predict that most of the Ca II resonance line and infrared triplet emission arises in dense layers close to the star rather than in the wind. Na I resonance line emission requires either dense chromospheres or massive winds.

Adopting a plausible expansion velocity field, Hα emission levels suggest mass loss rates $\sim 10^{-8}\ M_\odot\ \mathrm{yr}^{-1}$ for most T Tauri stars, in reasonable agreement with independent analysis of forbidden emission lines. Mass-loss rates $\gtrsim 10^{-7}\ M_\odot\ \mathrm{yr}^{-1}$ are required to produce broad blueshifted Na I resonance line absorption, in agreement with the results of Natta and Giovanardi. Since blueshifted Na I absorption is rather rare, we infer that the mass-loss rates for most TTS are $< 10^{-7}\ M_\odot\ \mathrm{yr}^{-1}$.

Subject headings: stars: emission-line — stars: pre–main-sequence — stars: winds

I. INTRODUCTION

Mass loss probably plays an important role during early stellar evolution. Winds may be needed to carry away angular momentum during star formation (Hartmann and MacGregor 1982; Pudritz and Norman 1983; Xhu *et al.* 1988), and it has been suggested that mass ejection may actually halt the accretion of material onto protostars (Shu and Terebey 1984). The observed high-velocity flows from pre–main-sequence objects in star-forming clouds (e.g., Kutner *et al.* 1982; Edwards and Snell 1982; Calvet, Cantó, and Rodríguez 1983) may have an important effect on conditions in molecular clouds (Lada 1985) and may help trigger further star formation (Norman and Silk 1980). The process producing these pre–main-sequence outflows is not clear; several mechanisms have been proposed (DeCampli 1981; Hartmann, Edwards, and Avrett 1982, hereafter HEA; Lago 1979, 1984; Hartmann and MacGregor 1982; Pudritz and Norman 1983; Croswell, Hartmann, and Avrett 1987; Shu *et al.* 1988; Pringle 1989).

In this context the winds of T Tauri (TT) stars are of particular interest. While the mass ejection during the TT phase may not represent the most energetic outflow of pre–main-sequence evolution, a variety of spectral diagnostics can be used to constrain acceleration mechanisms (Herbig 1962; Kuhi 1964; Schneeberger *et al.* 1979; Hartmann 1982; Mundt 1984; Appenzeller, Jankovics, and Ostreicher 1984; Edwards *et al.* 1987). Furthermore, TT stars are surprisingly slow rotators (Vogel and Kuhi 1981; Bouvier *et al.* 1986; Hartmann *et al.* 1986; Hartmann and Stauffer 1988), even though these stars may be accreting substantial amounts of high angular momentum disk material (Lynden-Bell and Pringle 1974; Bertout 1989; Kenyon and Hartmann 1987; Bertout, Basri, and Bouvier 1988). Thus studies of TT winds may help shed light on both mass-loss and angular momentum loss mechanisms in early stellar evolution.

Despite the large number of spectral lines that may be used to investigate the properties of TT outflows, these winds remain poorly understood. Part of the difficulty is the evident complexity of the line profiles, which indicate time variability, infall as well as outflow, etc. (cf. Hartmann 1982; Mundt 1984). The principal problem has been the scarcity of serious theoretical efforts to model observations. The interpretation of lines formed in the wind acceleration region requires the simultaneous solution of radiative transfer and statistical equilibrium equations for expanding atmospheres. One cannot assume hydrostatic equilibrium, radiative equilibrium, local thermodynamic equilibrium, or other usual simplifying approximations usually made in model atmosphere calculations. It is necessary to construct a grid of models to explore parameter space, a time-consuming task. Only recently has a grid of wind models for TTS been constructed to examine the effects of wind temperatures, mass loss rates, and velocity laws (Natta, Giovanardi, and Palla 1988). The work by Natta, Giovanardi, and Palla (1988), is very valuable, but is not exhaustive, because lines of ions other than hydrogen were not considered. Furthermore, line profiles were not calculated, despite the fact that profiles constrain velocity fields and therefore acceleration mechanisms.

In this paper we compute line fluxes and profiles for a sequence of spherically symmetric wind models. Our results for a series of relatively simple wind models should be useful for interpreting observed line profiles in terms of wind densities, temperatures, and velocity fields, with a view toward ultimately identifying the mechanism producing TT outflows. In a subsequent paper (Calvet and Hartmann 1990, hereafter Paper II), we relax the assumption of spherical geometry, consider the effects of disk occultation on line profiles, and investigate the possibility of accretion driven winds for TTS, either from a disk or from the boundary layer.

[1] Harvard-Smithsonian Center for Astrophysics.
[2] Centro de Investigaciones de Astronomia, Mérida, Venezuela.
[3] Grup d'Astrofisica de la Societat Catalana de Fisica (Institut d'Estudis Catalans).

In § II we describe the atmospheric structure of the wind models and the radiative transfer methods used. In § III we present results for line fluxes and profiles, and we present our conclusions for spherically symmetric flow in § IV.

II. MODEL CALCULATIONS

a) Wind Models

We make some restrictive assumptions in the wind models in order to make our task more manageable. The central star is assumed to have a radius of 3 $R_\odot$, a mass of 1 $M_\odot$, and an effective temperature of 4000 K, typical of pre–main-sequence objects in Taurus-Auriga (Cohen and Kuhl 1979). We assume spherically symmetric steady flow. While the complexity and variability of some TT line profiles indicates these assumptions are not always correct, many TTS do have relatively stable Hα profiles, and in any event we are concerned with representing the general behavior of TTS rather than modeling a specific star.

For our basic wind models we adopt velocity fields from the hydrodynamic calculations of HEA (model 5), in which the wind is driven by Alfvén waves in a radial magnetic geometry. This model differs qualitatively from most prior wind calculations in that large turbulent velocities are present, which are probably required to explain observed line profiles (see § IV). (Models in which the turbulent velocities are negligible have already been calculated by Natta, Giovanardi, and Palla 1988 for the hydrogen lines; see also Kuhl 1964 and Kuan 1975). The use of a hydrodynamic model ensures that our expansion and turbulent velocity fields are at least mutually self-consistent; the turbulent pressure drives the outflow in these low-temperature winds (Lago 1979, 1984; DeCampli 1981; HEA). The resulting expansion velocity rises from zero at the stellar surface to about 200 km s^{-1} at a distance of about $3R_*$ (see Fig. 1), consistent with the asymptotic flow velocities inferred from forbidden-line observations (Appenzeller, Jankovics, and Ostreicher 1984; Edwards *et al.* 1987). These expansion properties are typical of wind models in general and thus are not likely to significantly restrict the applicability of our results. The effects of differing expansion velocity gradients have been explored by Natta, Giovanardi, and Palla (1988) for the hydrogen lines.

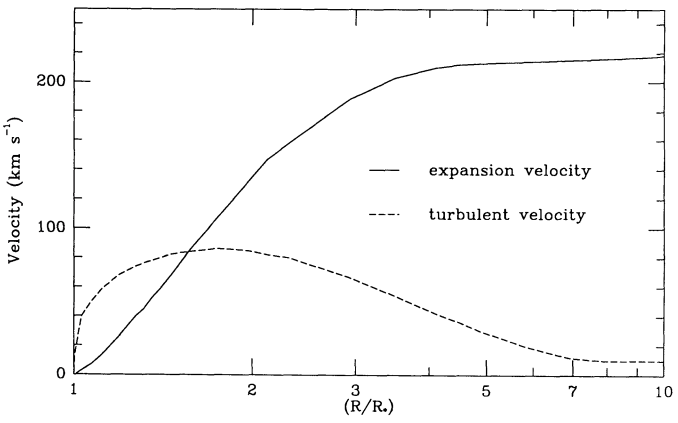

FIG. 1.—Expansion and turbulent velocity fields used for the wind model radiative transfer calculations. The velocities are taken from the hydrodynamic calculations of HEA (model 5). The turbulent velocities represent angle- and time-averaged Alfvén waves propagating through the envelope. The gradient in Alfvén wave pressure drives the outflow in these low-temperature winds (see § II; HEA).

The propagating Alfvén waves are highly supersonic in the inner wind regions where most of the line emission occurs, causing significant broadening of the line profiles (HEA). For simplicity we model the broadening as an isotropic and Gaussian microturbulent velocity field, calculating the velocity width from the wave amplitude in the wind model suitably averaged over wave period and angle (HEA). In reality the Alfvén waves must be transverse to the radial field lines, although other MHD wave modes may well be present without this restriction, especially close to the photosphere. The effect of tangential wave motions on the line profiles is considered briefly in § IV.

The temperature structure of the wind cannot be derived from theory because the dissipation mechanisms are not known. However, because wind temperatures are so low (see Hartmann 1986 for a review), thermal gas pressure does not have much effect on wind acceleration, and so we may consider differing ad hoc temperature structures using the same velocity field. Although emission from gas with temperatures 10^5–10^7 K is observed from TTS (Feigelson and DeCampli 1981; Gahm 1980; Imhoff and Giampapa 1980; Cram, Giampapa, and Imhoff 1980; Brown, Ferraz, and Jordan 1984), the emission measure of such gas is much smaller than that of TT winds (cf. DeCampli 1981; Hartmann 1986), and the observed optical indicators of outflow (Hα, Ca II) cannot be formed in such hot regions.

All models assumed the same photospheric structure, appropriate for a $T_{\rm eff}$ = 4000 K, log g = 3.5 star. Gas densities from the hydrodynamic wind model were somewhat arbitrarily interpolated to photospheric values. A temperature minimum of 3670 K was adopted at a distance of 2000 km above the photospheric level where $T = T_{\rm eff}$. The temperature was assumed to increase outward steeply from the temperature minimum until rapidly expanding layers of the wind were reached, in an attempt to mimic "chromospheric" models (e.g., Cram 1979; Calvet, Basri, and Kuhi 1984, hereafter CBK). The chromospheric temperature gradients were not the same in all models. As discussed below, the "deep chromosphere" regions are responsible for much of the Ca II emission and possibly the Na I emission.

Wind model 1 (see Table 1) has the temperature structure of wind model 5 of HEA, determined from balancing wave heating, radiative cooling, and adiabatic expansion, joined to a chromosphere as indicated in Figure 2. The same chromospheric structure was used for a sequence of "isothermal" wind models (models 2, 3, 4, 6, 7, 8, and 21; see Table 1). The isothermal wind was attached to the chromosphere essentially where the chromospheric temperature matched the final wind temperature (see Fig. 2). The density structure was changed to reflect the mass-loss rate as shown in Figure 2. Model 9 is the same as model 1, except that it has a denser and hotter chromosphere (Fig. 2). A further series of nonisothermal wind models was constructed; the temperature structures of models 12, T4, 15, and 19 are indicated in Figure 3, and detailed properties of models 12, T4, and 15 are provided in Tables 2–4.

b) Radiative Transfer Methods

Radiative transfer solutions for hydrogen lines and continua, and lines of Ca II, Mg II, and Na I were carried out with the Pandora computer program assuming spherical geometry

TABLE 1

SUMMARY OF WIND MODEL RESULTS

Number[a]	$\dot{M}$	T or T_{max}	F(Hα)	F(Hβ)	F(Hγ)	Mg II (k)	Ca II (K)	Ca II (IR)
1	6.5E − 9	3.4E4	4.2E7	1.1E7	6.0E6	2.6E8	1.2E7	−4.0E6
2(I)	6.5E − 9	2.0E4	5.2E7	1.3E7	6.3E6	4.3E8	1.3E7	−3.4E6
3(I)	6.5E − 9	1.0E4	3.3E7	4.5E6	1.3E6	2.0E8	1.1E7	−4.1E6
4(I)	1.0E − 7	5.0E3	−5.3E6	−1.7E7	−6.8E5	2.1E7	8.7E6	−5.6E6
6(I)	1.0E − 7	1.0E4	1.1E9	2.2E8	9.1E7	5.9E9	7.6E7	1.1E7
7(I)	6.5E − 9	8.0E3	7.3E6	−1.7E6	−1.8E6	5.7E7	5.8E6	−4.3E6
8(I)	1.0E − 7	8.0E3	6.1E8	1.0E8	4.5E7	1.5E9	5.1E7	1.5E7
9	6.5E − 9	3.4E4	4.3E7	1.1E7	5.4E6	2.8E8	2.6E7	−1.4E6
12(M)	1.0E − 8	1.0E4	5.0E7	6.1E6	1.5E6	3.5E8	1.9E7	−9.6E5
15	1.0E − 7	1.0E4	2.7E8	1.6E8	1.2E8	1.0E9	1.0E8	2.5E7
19	1.0E − 8	1.0E4	1.4E7	1.5E7	1.4E7	1.1E8	4.9E7	2.4E6
21(I)	1.0E − 7	2.0E4	1.5E9	3.7E8	1.7E8	9.7E9	2.3E8	2.9E7
T4(M)	1.0E − 8	3.4E4	9.6E7	2.0E7	9.0E6	...	...	...

NOTES.—Values are given in terms of base 10 exponents, i.e., 1E4 = 1×10^4. $\dot{M}$ is the mass-loss rate in solar masses per year; fluxes are in units of ergs cm^{-2} s^{-1}. Negative values indicate an absorption line.

[a] (I) indicates an isothermal wind model; (M) denotes moving source function calculation, as described in the text.

(Avrett and Loeser 1984). We adopted an eight-level hydrogen atom, with supplementary levels 9–12 added to improve the ionization balance. For Mg II we adopted a three-level model atom, including only the k line and the λ2790 subordinate line. The Ca II model atom also had three levels, including only the K line and the strongest infrared triplet line. We carried out tests with models having additional energy levels and transitions, and found that the three-level Mg II and Ca II models give adequate results for our purposes here. The Ca II and Mg II cross section data used in these calculations are taken from Shine (1973). Our Na I model atom consisted of eight levels; the D_1 and D_2 transitions were calculated separately.

Three basic methods were used to solve the non–LTE equations of statistical equilibrium. For an initial survey of the parameter dependence of the models we used escape probability methods to determine the level populations. The standard Sobolev escape probabilities (Castor 1970) were used in the outer, rapidly expanding regions of the wind. In the inner, low-expansion regions, we used probabilities of the form

$$\rho_{ij} \sim \frac{1}{1 + \tau_{ij}},$$

where τ_{ij} is the line center optical depth for transition ij (see Avrett and Loeser 1987 for details). A smooth transition between the Sobolev and static forms of ρ_{ij} is made between two selected radial points (-1.19×10^6 and -5.67×10^5 km, the same radii for all transitions). This transition region occurs where the turbulent velocities of the model are comparable to the expansion velocities. We term these models "escape probability" for short in the following discussion. The escape probability method was used for all of the hydrogen, Mg II, and Ca II calculations for models 1–4, 6–9, 15, 19, and 21.

The escape probability methods require that the line source

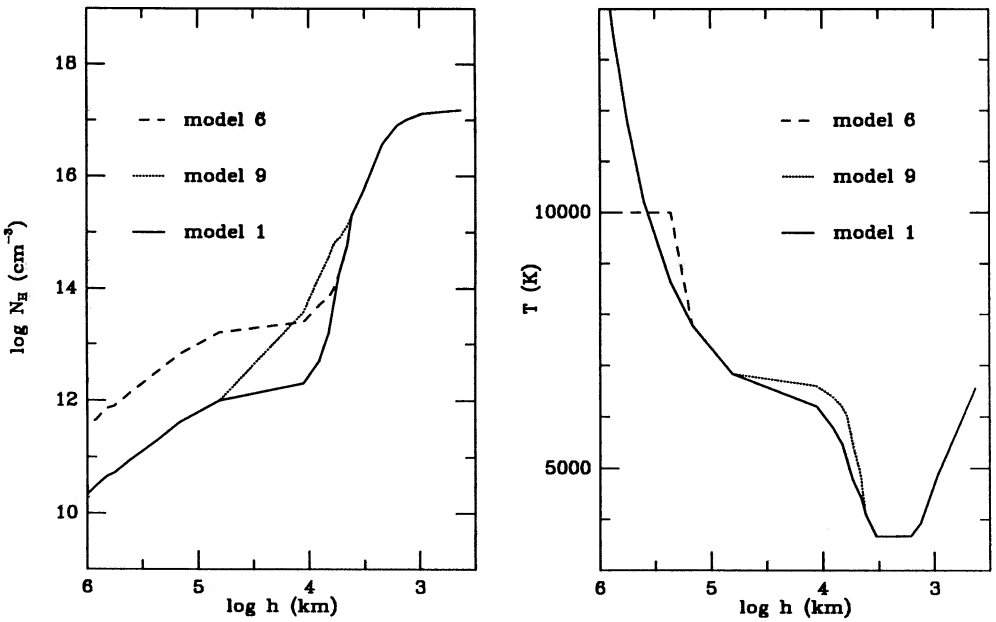

FIG. 2.—Density (*left*) and temperature (*right*) structures near the star for models 1, 6, and 9, showing the adopted chromospheric properties and the manner of joining isothermal wind models such as model 6 to the base chromosphere. The height scale is measured from the bottom of the photosphere and increases outward.

TABLE 2

HYDROGEN LEVEL POPULATIONS FOR MODEL 12

Depth (km)	T(K)	v(turb) (km/s)	v(exp) (km/s)	Electron Density	Hydrogen Density	Protons (1/cm3)	Level 1 (1/cm3)	Level 2 (1/cm3)	Level 3 (1/cm3)	Level 4 (1/cm3)	Level 5 (1/cm3)	Level 6 (1/cm3)	Level 7 (1/cm3)	Level 8 (1/cm3)
-2.19e+07	5000	10.0	219.0	8.12e+05	1.79e+08	5.15e+05	1.78e+08	1.22e-04	1.04e-09	8.84e-12	1.22e-12	1.67e-12	1.92e-13	6.83e-09
-1.89e+07	5000	10.0	218.0	9.93e+05	2.36e+08	6.12e+05	2.35e+08	1.76e-04	1.55e-09	1.63e-11	5.30e-12	7.36e-12	2.47e-12	9.02e-09
-1.69e+07	5000	10.0	217.0	1.13e+06	2.89e+08	6.68e+05	2.88e+08	2.17e-04	3.73e-09	2.74e-11	9.42e-12	1.21e-11	2.95e-11	1.10e-08
-1.44e+07	5000	10.0	216.0	1.47e+06	3.86e+08	8.72e+05	3.85e+08	3.31e-04	9.80e-09	1.43e-10	2.67e-10	3.63e-10	4.57e-10	1.48e-08
-1.23e+07	5000	12.0	215.0	2.28e+06	5.13e+08	1.56e+06	5.11e+08	5.67e-04	3.49e-08	1.98e-08	2.69e-08	3.73e-08	5.03e-08	5.98e-08
-1.02e+07	5300	19.0	214.0	3.99e+06	7.01e+08	2.93e+06	6.98e+08	1.71e-03	1.52e-07	6.25e-08	8.23e-08	1.13e-07	1.51e-07	1.77e-07
-8.14e+06	5950	30.0	213.0	1.51e+07	1.02e+09	1.35e+07	1.01e+09	2.67e-02	7.09e-06	1.14e-06	1.35e-06	1.79e-06	2.36e-06	2.70e-06
-7.31e+06	6440	36.0	212.0	5.41e+07	1.21e+09	5.21e+07	1.16e+09	3.49e-01	9.90e-05	1.59e-05	1.79e-05	2.35e-05	3.06e-05	3.45e-05
-6.47e+06	6900	42.0	210.0	2.08e+08	1.47e+09	2.05e+08	1.27e+09	5.05e+00	1.56e-03	2.52e-04	2.69e-04	3.47e-04	4.46e-04	4.96e-04
-5.22e+06	7790	54.0	203.0	9.44e+08	2.09e+09	9.41e+08	1.15e+09	9.63e+01	5.21e-02	6.06e-03	5.67e-03	7.01e-03	8.74e-03	9.56e-03
-4.00e+06	9000	67.0	188.0	2.56e+09	3.26e+09	2.54e+09	7.24e+08	6.00e+02	9.46e-01	8.04e-02	5.30e-02	5.65e-02	6.44e-02	6.72e-02
-2.73e+06	10500	80.0	158.0	6.19e+09	6.15e+09	5.73e+09	4.18e+08	2.58e+03	1.22e+01	8.49e-01	3.99e-01	3.69e-01	3.83e-01	4.06e-01
-2.34e+06	11200	82.0	147.0	8.25e+09	7.85e+09	7.52e+09	3.34e+08	3.98e+03	2.64e+01	1.93e+00	8.24e-01	7.16e-01	7.23e-01	7.70e-01
-1.97e+06	11400	85.0	129.0	1.14e+10	1.07e+10	1.03e+10	3.56e+08	6.65e+03	6.23e+01	5.16e+00	2.02e+00	1.65e+00	1.64e+00	1.78e+00
-1.55e+06	11400	86.0	107.0	1.71e+10	1.60e+10	1.56e+10	4.14e+08	1.21e+04	1.71e+02	1.83e+01	7.31e+00	5.89e+00	5.92e+00	6.51e+00
-1.19e+06	11200	84.0	85.3	2.59e+10	2.45e+10	2.39e+10	5.60e+08	2.17e+04	4.43e+02	6.03e+01	2.45e+01	1.91e+01	1.98e+01	2.26e+01
-9.45e+05	10670	82.0	67.4	3.69e+10	3.65e+10	3.53e+10	1.16e+09	3.64e+04	9.49e+02	1.53e+02	6.69e+01	5.32e+01	5.59e+01	6.47e+01
-8.40e+05	10240	80.0	59.4	4.33e+10	4.45e+10	4.26e+10	1.94e+09	4.66e+04	1.33e+03	2.31e+02	1.06e+02	8.64e+01	9.17e+01	1.07e+02
-7.45e+05	9940	78.0	53.1	5.03e+10	5.28e+10	4.99e+10	2.87e+09	5.74e+04	1.76e+03	3.23e+02	1.57e+02	1.33e+02	1.44e+02	1.68e+02
-6.51e+05	9650	76.0	45.0	6.27e+10	6.73e+10	6.24e+10	4.85e+09	7.98e+04	2.59e+03	5.04e+02	2.58e+02	2.25e+02	2.48e+02	2.91e+02
-5.67e+05	9370	74.0	40.0	7.29e+10	8.04e+10	7.27e+10	7.67e+09	9.94e+04	3.32e+03	6.80e+02	3.66e+02	3.28e+02	3.63e+02	4.29e+02
-4.00e+05	8500	68.0	26.0	9.68e+10	1.41e+11	9.66e+10	4.44e+10	1.64e+05	5.44e+03	1.21e+03	7.15e+02	6.73e+02	7.55e+02	8.89e+02
-2.31e+05	7785	58.0	13.0	1.09e+11	3.24e+11	1.08e+11	2.16e+11	2.21e+05	6.64e+03	1.57e+03	9.91e+02	9.59e+02	1.08e+03	1.26e+03
-1.47e+05	7290	50.0	7.0	9.65e+10	6.47e+11	9.56e+10	5.51e+11	2.00e+05	5.52e+03	1.34e+03	8.66e+02	8.39e+02	9.36e+02	1.09e+03
-6.30e+04	6833	40.0	3.0	9.06e+10	1.63e+12	8.88e+10	1.54e+12	1.89e+05	4.97e+03	1.28e+03	8.36e+02	8.09e+02	8.98e+02	1.04e+03
-9.95e+03	6600	16.0	0.0	4.71e+11	3.70e+13	4.46e+11	3.66e+13	2.43e+06	7.11e+04	2.21e+04	1.68e+04	1.71e+04	1.92e+04	2.23e+04
-6.81e+03	6400	11.0	0.0	8.45e+11	1.60e+14	7.63e+11	1.59e+14	6.05e+06	1.83e+05	6.14e+04	4.81e+04	4.94e+04	5.55e+04	6.43e+04
-5.35e+03	6200	9.0	0.0	9.17e+11	3.70e+14	7.66e+11	3.69e+14	7.74e+06	2.13e+05	7.07e+04	5.49e+04	5.60e+04	6.27e+04	7.23e+04
-4.72e+03	6000	7.9	0.0	7.76e+11	6.40e+14	5.64e+11	6.39e+14	7.10e+06	1.60e+05	4.95e+04	3.73e+04	3.77e+04	4.19e+04	4.81e+04
-4.10e+03	5500	7.5	0.0	2.89e+11	7.70e+14	1.18e+11	7.70e+14	1.43e+06	1.81e+04	5.15e+03	3.68e+03	3.60e+03	3.93e+03	4.47e+03
-3.26e+03	4850	6.6	0.0	1.84e+11	1.30e+15	9.62e+09	1.30e+15	1.34e+05	1.03e+03	2.90e+02	2.08e+02	2.02e+02	2.17e+02	2.42e+02
-2.81e+03	4100	5.9	0.0	1.68e+11	2.00e+15	1.40e+08	2.00e+15	2.30e+03	1.66e+01	4.65e+00	3.34e+00	3.18e+00	3.31e+00	3.60e+00
-2.00e+03	3670	4.7	0.0	1.39e+11	5.00e+15	1.12e+07	5.00e+15	2.81e+02	1.45e+00	2.54e-01	1.66e-01	1.49e-01	1.50e-01	1.60e-01
-8.60e+02	3670	2.9	0.0	5.03e+11	3.70e+16	2.00e+07	3.70e+16	1.46e+03	9.98e+00	2.69e+00	1.84e+00	1.66e+00	1.67e+00	1.78e+00
-3.00e+02	3676	0.0	0.0	8.30e+11	7.70e+16	2.36e+07	7.70e+16	3.21e+03	2.15e+01	5.79e+00	3.87e+00	3.42e+00	3.43e+00	3.65e+00
0.00e+00	3930	0.0	0.0	1.74e+12	1.00e+17	1.44e+08	1.00e+17	3.33e+04	2.65e+02	7.21e+01	4.79e+01	4.28e+01	4.35e+01	4.69e+01
3.85e+02	4848	0.0	0.0	9.70e+12	1.30e+17	7.36e+10	1.30e+17	1.30e+07	3.04e+05	1.10e+05	8.22e+04	7.95e+04	8.51e+04	9.51e+04
9.08e+02	6559	0.0	0.0	9.35e+13	1.50e+17	7.20e+13	1.50e+17	8.73e+09	6.95e+08	3.84e+08	3.49e+08	3.74e+08	4.27e+08	4.97e+08
1.33e+03	8008	0.0	0.0	8.84e+14	1.60e+17	8.50e+14	1.59e+17	2.43e+11	3.54e+10	2.41e+10	2.42e+10	2.74e+10	3.22e+10	3.83e+10

NOTES.—The depth scale is given relative to the stellar radius $R = 2.09 \times 10^6$ km. $V(\text{turb}) = V(t)$ is the microturbulent broadening velocity adopted, and $V(\text{exp}) = V(e)$ is the expansion velocity, both in km s^{-1}. All particle and atomic level densities are given in units of cm^{-3}. The upper level densities of hydrogen are uncertain in the first three or four depth points in the models due to difficulties in convergence, but these uncertainties have little effect on the line fluxes.

TABLE 3

HYDROGEN LEVEL POPULATIONS FOR MODEL T4

Depth (km)	T(K)	v(turb) (km/s)	v(exp) (km/s)	Electron Density	Hydrogen Density	Protons (1/cm3)	Level 1 (1/cm3)	Level 2 (1/cm3)	Level 3 (1/cm3)	Level 4 (1/cm3)	Level 5 (1/cm3)	Level 6 (1/cm3)	Level 7 (1/cm3)	Level 8 (1/cm3)
-2.19e+07	7920	10.0	219.0	2.08e+07	1.79e+08	1.39e+07	1.65e+08	2.96e-02	4.88e-07	6.66e-07	9.54e-07	1.33e-06	1.78e-06	2.12e-06
-1.89e+07	9020	10.0	218.0	9.02e+07	2.36e+08	1.22e+08	1.14e+08	1.55e+00	3.38e-05	4.18e-05	5.95e-05	8.21e-05	1.10e-04	1.31e-04
-1.69e+07	10300	10.0	217.0	1.66e+08	2.89e+08	2.30e+08	5.91e+07	4.87e+00	1.25e-04	1.27e-04	1.77e-04	2.43e-04	3.22e-04	3.85e-04
-1.44e+07	11900	10.0	216.0	2.88e+08	3.86e+08	3.62e+08	2.38e+07	9.15e+00	3.30e-04	2.50e-04	3.37e-04	4.57e-04	6.01e-04	7.15e-04
-1.23e+07	14300	12.0	215.0	5.38e+08	5.13e+08	5.09e+08	3.76e+06	6.80e+00	5.60e-04	3.63e-04	4.80e-04	6.44e-04	8.41e-04	1.00e-03
-1.02e+07	19400	19.0	214.0	8.34e+08	7.01e+08	7.00e+08	7.13e+05	2.62e+00	8.51e-04	6.75e-04	8.90e-04	1.18e-03	1.52e-03	1.80e-03
-8.14e+06	26950	30.0	213.0	1.22e+09	1.02e+09	1.02e+09	4.33e+05	2.87e+00	2.05e-03	1.62e-03	2.03e-03	2.59e-03	3.24e-03	3.80e-03
-7.31e+06	30260	36.0	212.0	1.45e+09	1.21e+09	1.21e+09	4.52e+05	4.34e+00	3.44e-03	2.46e-03	2.97e-03	3.67e-03	4.50e-03	5.22e-03
-6.47e+06	33520	42.0	210.0	1.77e+09	1.47e+09	1.47e+09	4.81e+05	6.89e+00	6.17e-03	4.00e-03	4.65e-03	5.61e-03	6.72e-03	7.74e-03
-5.22e+06	37670	54.0	203.0	2.51e+09	2.09e+09	2.09e+09	5.80e+05	1.59e+01	1.77e-02	9.28e-03	1.03e-02	1.21e-02	1.41e-02	1.62e-02
-4.00e+06	39450	67.0	188.0	3.92e+09	3.26e+09	3.26e+09	8.12e+05	4.44e+01	7.02e-02	2.45e-02	2.61e-02	3.00e-02	3.49e-02	4.06e-02
-2.73e+06	36200	80.0	158.0	7.39e+09	6.15e+09	6.15e+09	2.00e+06	3.19e+02	1.44e+00	1.32e-01	1.10e-01	1.19e-01	1.38e-01	1.64e-01
-2.34e+06	34050	82.0	147.0	9.43e+09	7.85e+09	7.85e+09	2.99e+06	6.39e+02	4.42e+00	2.96e-01	2.00e-01	2.08e-01	2.40e-01	2.87e-01
-1.97e+06	30030	85.0	129.0	1.28e+10	1.07e+10	1.07e+10	5.34e+06	1.56e+03	1.90e+01	1.21e+00	5.04e-01	4.63e-01	5.21e-01	6.25e-01
-1.55e+06	25320	86.0	107.0	1.90e+10	1.60e+10	1.60e+10	1.06e+07	4.07e+03	9.65e+01	9.82e+00	2.79e+00	1.88e+00	1.92e+00	2.25e+00
-1.19e+06	19060	84.0	85.3	2.70e+10	2.45e+10	2.45e+10	3.11e+07	9.38e+03	3.32e+02	4.85e+01	1.71e+01	1.11e+01	1.09e+01	1.28e+01
-9.45e+05	16700	82.0	67.4	4.01e+10	3.65e+10	3.64e+10	9.13e+07	1.87e+04	8.02e+02	1.31e+02	5.06e+01	3.61e+01	3.72e+01	4.39e+01
-8.40e+05	14370	80.0	59.4	4.88e+10	4.45e+10	4.42e+10	2.51e+08	2.78e+04	1.24e+03	2.15e+02	8.97e+01	6.84e+01	7.25e+01	8.60e+01
-7.46e+05	13500	78.0	53.1	5.78e+10	5.28e+10	5.24e+10	3.65e+08	3.53e+04	1.70e+03	3.18e+02	1.43e+02	1.15e+02	1.25e+02	1.48e+02
-6.51e+05	12630	76.0	45.0	7.34e+10	6.73e+10	6.68e+10	4.82e+08	4.69e+04	2.50e+03	5.12e+02	2.53e+02	2.18e+02	2.41e+02	2.88e+02
-5.67e+05	11800	74.0	40.0	8.68e+10	8.04e+10	7.99e+10	5.20e+08	5.82e+04	3.28e+03	7.21e+02	3.87e+02	3.49e+02	3.92e+02	4.68e+02
-4.00e+05	10210	68.0	26.0	1.38e+11	1.41e+11	1.38e+11	3.53e+09	1.31e+05	6.92e+03	1.76e+03	1.13e+03	1.12e+03	1.28e+03	1.53e+03
-2.31e+05	8630	58.0	13.0	2.26e+11	3.24e+11	2.35e+11	8.89e+10	3.86e+05	1.68e+04	4.79e+03	3.47e+03	3.57e+03	4.12e+03	4.88e+03
-1.47e+05	7780	50.0	7.0	1.85e+11	6.47e+11	1.95e+11	4.52e+11	4.36e+05	1.52e+04	4.13e+03	2.94e+03	2.99e+03	3.40e+03	4.00e+03
-6.30e+04	6833	40.0	3.0	8.60e+10	1.63e+12	8.34e+10	1.55e+12	1.90e+05	4.59e+03	1.07e+03	7.12e+02	6.98e+02	7.79e+02	9.03e+02
-9.95e+03	6600	16.0	0.0	4.77e+11	3.70e+13	4.54e+11	3.66e+13	2.41e+06	7.22e+04	2.27e+04	1.73e+04	1.77e+04	1.99e+04	2.31e+04
-6.82e+03	6400	11.0	0.0	8.81e+11	1.60e+14	8.08e+11	1.59e+14	5.97e+06	1.91e+05	6.70e+04	5.32e+04	5.48e+04	6.16e+04	7.13e+04
-5.35e+03	6200	9.0	0.0	9.82e+11	3.70e+14	8.47e+11	3.69e+14	7.60e+06	2.33e+05	8.24e+04	6.53e+04	6.69e+04	7.49e+04	8.64e+04
-4.72e+03	6000	7.9	0.0	8.72e+11	6.40e+14	6.83e+11	6.39e+14	6.94e+06	1.93e+05	6.58e+04	5.12e+04	5.19e+04	5.78e+04	6.63e+04
-4.10e+03	5500	7.5	0.0	3.17e+11	7.70e+14	1.52e+11	7.70e+14	1.41e+06	2.74e+04	7.70e+03	5.53e+03	5.41e+03	5.90e+03	6.70e+03
-3.26e+03	4850	6.6	0.0	1.88e+11	1.30e+15	1.41e+10	1.30e+15	1.32e+05	2.00e+03	5.27e+02	3.65e+02	3.46e+02	3.68e+02	4.11e+02
-2.81e+03	4100	5.9	0.0	1.68e+11	2.00e+15	1.94e+08	2.00e+15	2.30e+03	3.02e+01	8.04e+00	5.39e+00	4.89e+00	5.03e+00	5.46e+00
-2.00e+03	3670	4.7	0.0	1.39e+11	5.00e+15	1.69e+07	5.00e+15	1.97e+02	2.53e+00	6.72e-01	4.40e-01	3.87e-01	3.87e-01	4.13e-01
-8.60e+02	3670	2.9	0.0	5.03e+11	3.70e+16	2.48e+07	3.70e+16	1.45e+03	1.45e+01	3.95e+00	2.52e+00	2.20e+00	2.19e+00	2.34e+00
-3.00e+02	3676	0.0	0.0	8.30e+11	7.70e+16	2.76e+07	7.70e+16	3.20e+03	2.82e+01	7.53e+00	4.76e+00	4.14e+00	4.13e+00	4.40e+00
0.00e+00	3930	0.0	0.0	1.74e+12	1.00e+17	1.60e+08	1.00e+17	3.33e+04	3.14e+02	8.40e+01	5.44e+01	4.82e+01	4.89e+01	5.28e+01
3.85e+02	4848	0.0	0.0	9.70e+12	1.30e+17	7.51e+10	1.30e+17	1.30e+07	3.08e+05	1.12e+05	8.40e+04	8.12e+04	8.70e+04	9.72e+04
9.08e+02	6559	0.0	0.0	9.34e+13	1.50e+17	7.19e+13	1.50e+17	8.73e+09	6.94e+08	3.83e+08	3.48e+08	3.74e+08	4.26e+08	4.96e+08
1.33e+03	8008	0.0	0.0	8.84e+14	1.60e+17	8.50e+14	1.59e+17	2.43e+11	3.54e+10	2.41e+10	2.42e+10	2.74e+10	3.22e+10	3.83e+10

NOTE.—See Note to Table 2.

TABLE 4

HYDROGEN AND Na LEVEL POPULATIONS FOR MODEL 15

Depth(km)	T(K)	v(t) (km/s)	v(e) (km/s)	Electron Density	Hydrogen Density	Protons (1/cm3)	N(H) 1 (1/cm3)	N(H) 2 (1/cm3)	N(H) 3 (1/cm3)	N(Na II) (1/cm3)	N(Na) 1 (1/cm3)	N(Na) 2 (1/cm3)	N(Na) 3 (1/cm3)
-2.19e+07	5000	10	219.0	2.80e+06	1.79e+09	3.47e+05	1.79e+09	1.70e-03	6.80e-09	3.83e+03	2.34e-03	8.06e-08	1.59e-07
-1.89e+07	5000	10	218.0	8.03e+06	2.36e+09	4.55e+06	2.36e+09	3.05e-02	1.72e-07	5.05e+03	6.59e-03	2.97e-07	5.85e-07
-1.69e+07	5000	10	217.0	1.16e+07	2.98e+09	7.00e+06	2.97e+09	5.29e-02	3.75e-07	6.37e+03	9.48e-03	5.27e-07	1.05e-06
-1.44e+07	5000	10	216.0	1.50e+07	3.86e+09	9.67e+06	3.85e+09	6.97e-02	6.86e-07	8.25e+03	1.15e-02	8.46e-07	1.68e-06
-1.23e+07	5000	12	215.0	2.46e+07	5.13e+09	1.82e+07	5.11e+09	1.66e-01	2.26e-06	1.10e+04	1.87e-02	1.81e-06	3.60e-06
-1.02e+07	5000	19	214.0	4.55e+07	7.01e+09	4.07e+07	6.97e+09	5.66e-01	1.12e-05	1.50e+04	3.36e-02	4.51e-06	8.97e-06
-8.14e+06	5000	30	213.0	8.88e+07	1.02e+10	8.13e+07	1.01e+10	1.46e+00	4.65e-05	2.18e+04	5.75e-02	1.18e-05	2.47e-05
-7.31e+06	5000	36	212.0	1.47e+08	1.21e+10	1.35e+08	1.20e+10	3.28e+00	1.36e-04	2.59e+04	9.14e-02	2.21e-05	4.57e-05
-6.47e+06	5400	42	210.0	4.52e+08	1.47e+10	4.16e+08	1.43e+10	2.33e+01	1.69e-03	3.14e+04	2.51e-01	7.30e-05	1.50e-04
-5.22e+06	6000	54	203.0	1.52e+09	2.09e+10	1.49e+09	1.94e+10	1.93e+02	9.85e-02	4.47e+04	6.94e-01	2.80e-04	5.73e-04
-4.00e+06	6600	67	188.0	6.39e+09	3.26e+10	6.34e+09	2.63e+10	1.68e+03	1.22e+01	6.97e+04	1.70e+00	1.31e-03	2.95e-03
-2.73e+06	7300	80	158.0	2.55e+10	6.15e+10	2.54e+10	3.60e+10	1.34e+04	6.61e+02	1.31e+05	6.43e+00	7.03e-03	1.50e-02
-2.34e+06	8000	82	147.0	5.70e+10	7.85e+10	5.69e+10	2.16e+10	3.40e+04	2.50e+03	1.68e+05	1.27e+01	1.64e-02	3.44e-02
-1.97e+06	9000	85	129.0	1.00e+11	1.07e+11	1.00e+11	6.87e+09	5.49e+04	4.45e+03	2.29e+05	1.89e+01	2.95e-02	6.17e-02
-1.55e+06	9600	86	107.0	1.57e+11	1.60e+11	1.56e+11	3.65e+09	6.54e+04	6.12e+03	3.42e+05	1.77e+01	4.41e-02	9.28e-02
-1.19e+06	10000	84	85.3	2.42e+11	2.45e+11	2.41e+11	3.67e+09	1.06e+05	9.98e+03	5.24e+05	2.87e+01	8.45e-02	1.77e-01
-9.45e+05	10000	82	67.4	3.60e+11	3.65e+11	3.59e+11	6.06e+09	1.79e+05	1.66e+04	7.80e+05	4.56e+01	1.59e-01	3.31e-01
-8.40e+05	10000	80	59.4	4.39e+11	4.45e+11	4.37e+11	7.64e+09	2.29e+05	2.13e+04	9.51e+05	5.52e+01	2.13e-01	4.44e-01
-7.45e+05	10000	78	53.1	5.21e+11	5.28e+11	5.20e+11	7.86e+09	2.33e+05	2.31e+04	1.13e+06	3.41e+01	2.01e-01	3.89e-01
-6.51e+05	10000	76	45.0	6.63e+11	6.73e+11	6.62e+11	1.12e+10	3.37e+05	3.33e+04	1.44e+06	5.24e+01	3.15e-01	6.16e-01
-5.67e+05	10000	74	40.0	7.91e+11	8.04e+11	7.90e+11	1.45e+10	4.35e+05	4.32e+04	1.72e+06	7.04e+01	4.32e-01	8.58e-01
-4.00e+05	10000	68	26.0	1.38e+12	1.41e+12	1.38e+12	3.25e+10	9.71e+05	1.00e+05	3.01e+06	1.69e+02	1.14e+00	2.36e+00
-2.31e+05	8600	58	13.0	2.43e+12	3.24e+12	2.42e+12	8.17e+11	3.51e+06	3.50e+05	6.93e+06	7.41e+02	5.68e+00	1.25e+01
-1.47e+05	7786	50	7.0	2.20e+12	6.47e+12	2.19e+12	4.28e+12	4.32e+06	3.88e+05	1.38e+07	1.80e+03	1.37e+01	3.02e+01
-6.30e+04	6833	40	3.0	1.00e+12	1.63e+13	9.91e+11	1.53e+13	1.85e+06	1.44e+05	3.48e+07	4.51e+03	2.48e+01	5.30e+01
-2.10e+04	6205	34	0.0	4.44e+11	2.50e+13	4.31e+11	2.46e+13	5.12e+05	4.51e+04	5.34e+07	5.68e+03	2.03e+01	3.97e+01
-1.28e+04	5800	28	0.0	3.06e+11	4.90e+13	2.88e+11	4.87e+13	2.65e+05	2.67e+04	1.05e+08	9.87e+03	2.89e+01	5.29e+01
-1.08e+04	5460	15	0.0	1.90e+11	7.00e+13	1.73e+11	6.98e+13	1.04e+05	1.25e+04	1.50e+08	9.65e+03	2.61e+01	4.61e+01
-8.80e+03	5120	5	0.0	1.10e+11	1.00e+14	9.24e+10	9.99e+13	3.34e+04	4.77e+03	2.14e+08	8.26e+03	2.27e+01	3.77e+01
-6.80e+03	4780	0	0.0	7.01e+10	1.80e+14	4.48e+10	1.80e+14	1.08e+04	1.72e+03	3.85e+08	1.01e+04	2.76e+01	4.55e+01
-4.80e+03	4440	0	0.0	8.97e+10	6.00e+14	1.59e+10	6.00e+14	5.52e+03	8.63e+02	1.28e+09	5.32e+04	1.32e+02	2.22e+02
-2.81e+03	4100	0	0.0	1.70e+11	2.00e+15	2.68e+09	2.00e+15	2.14e+03	3.04e+02	4.28e+09	7.13e+05	9.74e+02	1.81e+03
-2.00e+03	3670	0	0.0	1.39e+11	5.00e+15	2.41e+08	5.00e+15	1.79e+02	2.72e+01	1.07e+10	2.10e+06	2.44e+03	4.90e+03
-8.60e+02	3670	0	0.0	5.04e+11	3.70e+16	2.28e+08	3.70e+16	1.43e+03	1.13e+02	7.90e+10	7.81e+07	1.20e+05	2.40e+05
-3.00e+02	3676	0	0.0	8.31e+11	7.70e+16	1.51e+08	7.70e+16	3.18e+03	1.31e+02	1.64e+11	4.34e+08	6.12e+05	1.22e+06
0.00e+00	3930	0	0.0	1.74e+12	1.00e+17	4.47e+08	1.00e+17	3.33e+04	6.94e+02	2.13e+11	8.88e+08	1.83e+06	3.64e+06
3.85e+02	4848	0	0.0	9.70e+12	1.30e+17	7.95e+10	1.30e+17	1.30e+07	3.22e+05	2.77e+11	6.86e+08	4.48e+06	8.92e+06
9.08e+02	6559	0	0.0	9.34e+13	1.50e+17	7.19e+13	1.50e+17	8.74e+09	6.94e+08	3.20e+11	2.08e+08	5.04e+06	1.00e+07
1.33e+03	8008	0	0.0	8.84e+14	1.60e+17	8.50e+14	1.59e+17	2.43e+11	3.54e+10	3.42e+11	2.99e+08	1.42e+07	2.84e+07

NOTE.—See Note to Table 2.

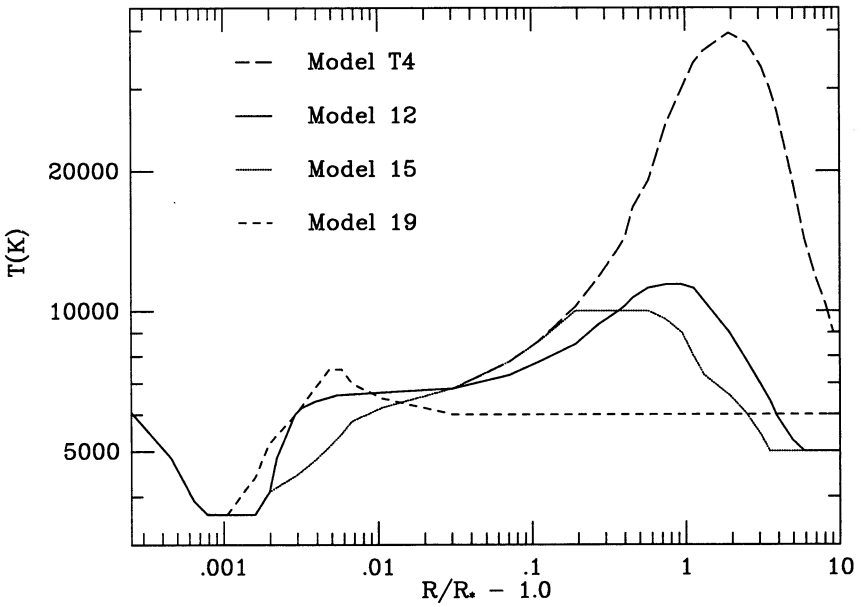

FIG. 3.—The adopted temperature structures for the nonisothermal wind models T4, 12, 15, and 19

function be relatively constant over the region of line formation, which may not always be true. Radiative transfer methods which explicitly account for the global nature of the solution have also been considered. Using the line transfer methods discussed by Avrett and Loeser (1984), we constructed line source functions for a spherically extended, expanding envelope model, incorporating the detailed velocity fields. This method is very expensive computationally, and so only two models of this type were calculated (models 12 and T4). However, comparison with the other methods indicates that the escape probability methods usefully illustrate trends and parameter dependencies.

For the "moving radiative transfer" (MRT) calculations, we solved the coupled line transfer equations for all transitions of an eight-level hydrogen atom, except for the Lyman lines. The source functions for the Lyman lines were calculated using the Sobolev/static escape probabilities discussed above. The Mg II *k* and Ca II K resonance lines were calculated with the partial redistribution methods described by Avrett and Loeser (1984).

The Na I source functions were calculated ignoring atmospheric expansion. Because Na I generally forms in layers where the broadening velocity is greater than or comparable to the expansion velocity, this approximation should not be too bad. The line profiles were calculated using the static source functions with the appropriate velocity field.

III. LINE FLUX RESULTS

Table 1 summarizes the basic grid of wind models and lists the emergent line fluxes. Hydrogen level populations and electron densities for the detailed moving radiative transfer (MRT) wind models 12 and T4 are presented in Tables 2 and 3. Hydrogen and Na I level populations are presented for the high mass-loss rate model 15 in Table 4. A discussion of source function behavior appears in the Appendix. Hydrogen ionization in such winds has been discussed by Natta, Giovanardi, and Palla (1988).

In the following discussion, we use the wind model fluxes as a guide to the densities, temperatures, and mass-loss rates of TT winds. In § IV we examine the implications of our line profile results for the magnitude and character of TT velocity fields.

a) Atmospheric Extension: the Balmer Decrement

Because emission line fluxes generally depend upon column densities and emission measures, one needs to estimate the size of the relevant emitting region in order to interpret line fluxes in terms of envelope densities. The Balmer decrement [$\equiv F(\mathrm{H}\alpha)/F(\mathrm{H}\beta)$] is a useful diagnostic in this regard. The observations (Fig. 4) show quite large decrements, well above case B recombination values, and this result should be relatively insensitive to uncertainties in reddening. "Chromospheric" models, i.e., models in which the hydrogen line emission arises from a plane-parallel layer, have not been able to explain large Balmer decrements (Cram 1979; CBK), whereas wind models have had some success (Kuan 1975; HEA; Natta, Giovanardi, and Palla 1988). Our models reinforce this conclusion (Fig. 4; note the decrement ~ 1 found for the chromospheric model 19). The enhancement of Hα relative to Hβ in the winds is not due to collisional effects, which dominate in all models, but to a larger volume of formation of Hα relative to Hβ (see Appendix). The only wind model which does not show a large decrement is model 15. The reason for this behavior is that Hβ is formed in an extended region in this dense wind, while the rapid fall-off in temperature in the outer layers prevents the Hα emission region from being much larger. The decrement is largest for model 7, in which Hβ is in absorption. The densities and temperatures in the envelope are too low to provide significant envelope emission. Thus very large Balmer decrements, with little or no emission in Hβ, indicate low envelope densities, and thus low mass-loss rates.

We conclude, as in HEA, that the large Balmer decrements observed require Hα to be formed in an extended envelope relative to the higher Balmer lines. This result should be kept in mind when considering observations which show that the Hα profiles can be qualitatively different than the Hβ, Hγ, etc. profiles in some TTS (e.g., Hartmann 1982). The models indi-

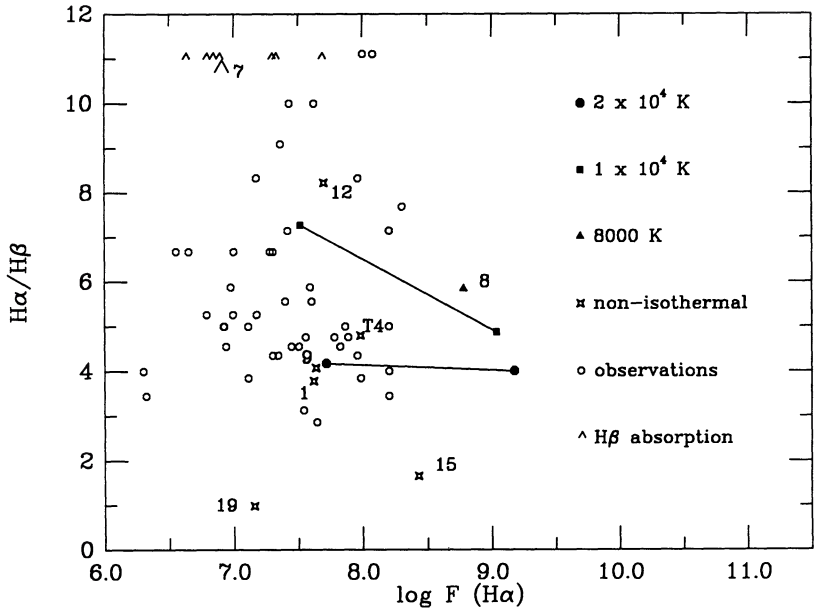

FIG. 4.—Hα/Hβ ratios produced by the wind models as a function of Hα line flux. In this and following figures the line flux F is measured in ergs cm^{-2} s^{-1} and is related to the line luminosity L by $F = L/(4\pi R^2)$, where the stellar radius is 3 $R_\odot$. The observed values are taken from Calvet and Albarrán (1984). The Λ symbol used for model 7 and for some of the observations indicates Hβ in absorption. Lines connect isothermal models with the same wind temperatures but differing mass-loss rates.

cate that Hα is mostly formed in a different region of the envelope than the higher Balmer series, and so can reflect a different velocity field in its line profile.

b) Dependence of Line Emission on $\dot{M}$ and T

Our model sequence indicates the dependence of line emission on relative mass-loss rate for a fixed expansion velocity field. The exact translation of our results into a specific mass-loss rate depends upon the appropriateness of the expansion velocity and can only be assessed using the line profiles, as discussed in § IV. However, we note that our results suggest $\dot{M} \sim 10^{-8}$ to 10^{-7} $M_\odot$ yr^{-1}, consistent with independent estimates made by Edwards *et al.* (1987) modeling the broad forbidden emission lines.

Table 1 and Figure 5 show that the Hα flux depends strongly on mass-loss rate, or equivalently on density since the expansion velocity is fixed. For a fixed wind temperature and expansion velocity, the Hα flux varies with mass-loss rate as $F \propto \dot{M}^n$, with $1.2 < n < 1.6$. A similar result holds for the Mg II resonance lines (see below). This dependence of line flux is very similar to the $\dot{M}^{4/3}$ expected on general grounds for LTE Sobolev wind models (Krolik and Smith 1981; Simon *et al.* 1983), and found to be roughly appropriate for the non-LTE hydrogen models of Natta, Giovanardi, and Palla (1988).

The Hα line fluxes are not very sensitive to temperature in the range (1–3) × 10^4 K. However, below 1 × 10^4 K the temperature dependence is quite steep, and at 5000 K the Hα line goes into *absorption*, even in a very dense wind (Table 1, model 4).

We emphasize that our results for the Balmer lines depend upon the assumed photospheric radiation field. Had we chosen a hotter photospheric temperature, the Hα equivalent widths would be smaller because of the important effects of the Balmer continuum radiation field on Hα formation (Jefferies and Thomas 1959). Thus a wind that produces Hα emission for a typical K7–M0 star (assumed here) may result in strong Hα *absorption* for a G star. Direct comparisons of the Balmer line emission of G-type and M-type TTS are not meaningful.

Comparison with observations indicates that wind temperatures generally need to be in excess of 8000 K in the innermost ($r \lesssim 3\ R_*$) regions in order to explain the Hα emission from stars with $T_{\rm eff} \sim 4000$ K. It is difficult to constrain the temperature more accurately than this. The observed range of

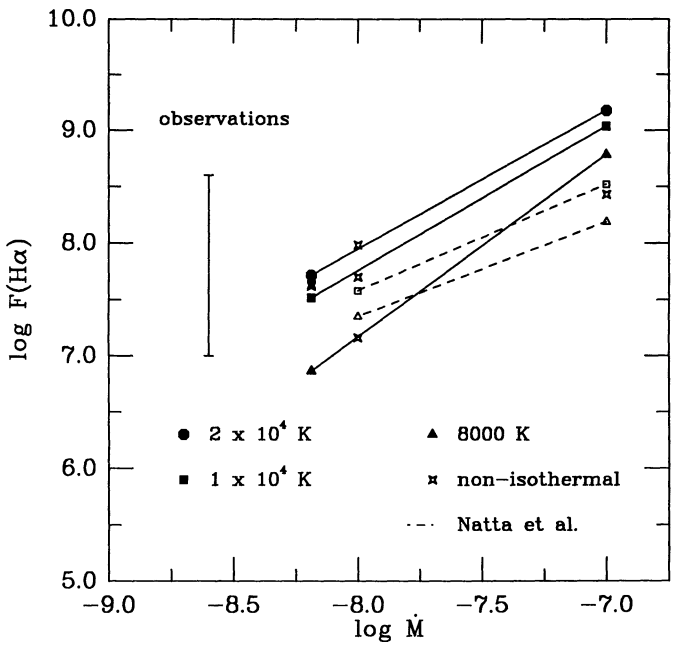

FIG. 5.—The dependence of model Hα emission in ergs cm^{-2} s^{-1} (normalized to the stellar surface, with radius 3 $R_\odot$) on mass-loss rate in $M_\odot$ yr^{-1}. Results from the models of Natta, Giovanardi, and Palla (1988) for 8000 K and 10,000 K winds are also shown (normalized to the radius of 7 $R_\odot$ used by Natta *et al.*). Lines connect isothermal models with the same wind temperatures.

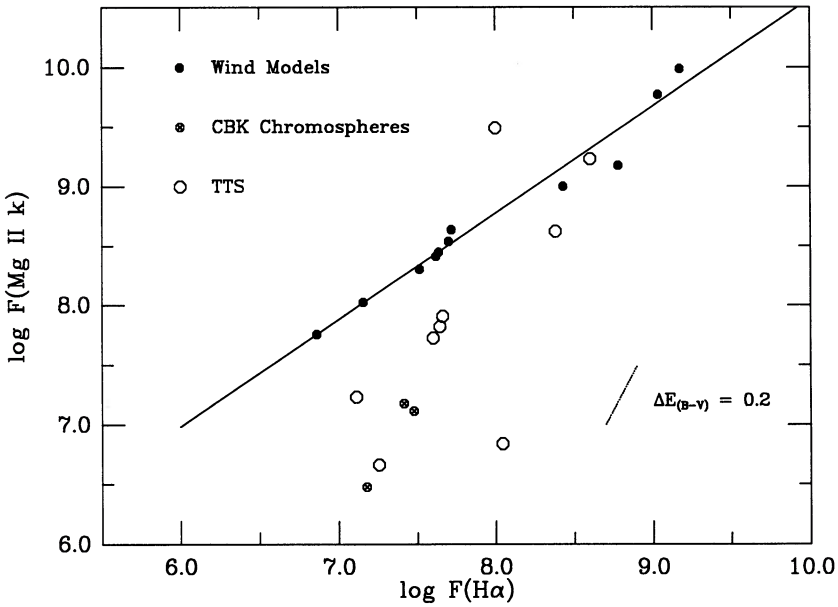

FIG. 6.—The relationship between Mg II *k* and Hα surface fluxes for the models. Lines connect isothermal models with the same wind temperatures. The results of the Calvet, Basri, and Kuhi (1984) chromospheric models are shown as crossed circles. A reddening vector of a change in $E(B-V)$ of 0.2 mag is shown, assuming the standard reddening law.

Hα schematically indicated in Figure 5 is restricted to line fluxes $\geq 1 \times 10^7$ ergs cm^{-2} s^{-1}. This lower limit corresponds to an equivalent width of about 5 Å for a 4000 K star. TTS of spectral types ~K7 or later with Hα equivalent widths $\lesssim 10$ Å exhibit narrow Hα profiles similar to those of dMe stars (~1 – 2 Å FWHM), quite unlike the wind model profiles (§ IV).

The models exhibit an extremely tight relationship between Mg II *k* versus Hα, as shown in Figure 6. The relationship applies to both isothermal and nonisothermal wind models, and even to our very dense chromospheric model (model 19). The observed relation between Mg II *k* and Hα (Calvet *et al.* 1985; Calvet and Albarrán 1984) shows considerable scatter and is strongly dependent upon the values of extinction adopted. In Figure 5 and Table 5 we have taken A_v from Strom *et al.* (1988), resulting in substantially larger reddening corrections than those adopted by Calvet *et al.* (1985). Although the chromospheric models of CBK produce Hα/Mg II ratios in better agreement with the many of the observations, the CBK chromosphere models do not reproduce the observed large Hα/Hβ ratios. The Balmer decrement is probably a stronger constraint on the models, since it is far less dependent upon reddening corrections.

TABLE 5

EXTINCTION-CORRECTED Hα, Mg II, AND Ca II FLUXES FOR SELECTED T TAURI STARS

Star	A_v	F(Mg II)	F(Ca II)	F(Hα)
BP Tau	0.5	1.7E7	2.3E7	1.3E7
DE Tau	0.6	4.6E6	1.5E7	1.8E7
RY Tau	1.9	8.1E7	1.8E7	4.6E7
T Tau	1.4	5.3E7	4.3E7	4.0E7
DF Tau	1.9	6.6E7	8.1E7	4.4E7
DG Tau	4.0	3.1E9	6.1E8	1.0E8
DR Tau	3.3	1.7E9	6.6E8	4.0E8
GM Aur	0.3	6.9E6	2.8E7	1.1E8
RW Aur	1.3	4.2E8	5.8E8	2.4E8

NOTES.—Surface fluxes are in units of ergs cm^{-2} s^{-1}. Reddening values are taken from Strom *et al.* 1988; Mg II and Ca II fluxes are taken from Calvet *et al.* 1985; Hα fluxes from Calvet and Albarran 1984.

Recent studies of blue veiling in TTS suggest that the effects of the veiling continuum on the optical spectra have been underestimated. Hartigan *et al.* (1989) and Hartmann and Kenyon (1990) argue that the veiling present in TTS generally causes $V-R$ colors to be about 0.2–0.3 mag too blue. This would produce an underestimate of the reddening at 2800 Å of more than 1 mag, improving the agreement between models and observations.

c) Ca II *and* Na I *Line Formation*

Because calcium ionizes to Ca III at relatively low densities and temperatures, the emission fluxes tend to be produced more in high-density deep "chromosphere" regions than in the extended winds. This is shown by a comparison between models 1 and 9 (Table 1). The Balmer and Mg II fluxes are little changed, but the Ca II resonance line emission increases by a factor of 2 in model 9, which has the same wind structure but a denser chromosphere than model 1 (Fig. 2).

As shown in Figure 7, the Ca II K emission depends very little on wind temperature for the lower mass-loss rates, simply because the ionization effects effectively eliminate the contribution of wind regions to the resonance line flux. Only at high mass-loss rates (10^{-7} $M_\odot$ yr^{-1}) is a substantial fraction of the Ca II K flux produced in the wind.

Figure 8 compares theoretical fluxes for Ca II K and Mg II *k* with the nearly simultaneous observations of Calvet *et al.* (1985; corrected for reddening using the values of extinction estimated by Strom *et al.* 1988). The models define a locus parallel to the reddening vector, and so the discrepancy between models and observations cannot be explained by extinction.

The deep chromosphere model 19 exhibits a ratio of Ca II K/Mg II *k* in reasonable agreement with observations (Fig. 8). However, plane-parallel models are not acceptable for the hydrogen lines because of the small Hα/Hβ ratios that result.

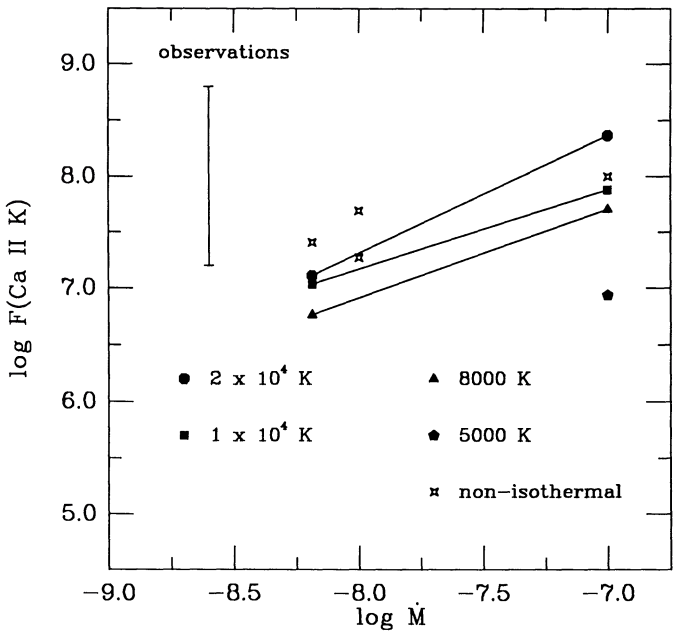

FIG. 7.—Dependence of Ca II K flux on mass-loss rate for differing wind temperatures. Lines connect isothermal models with the same wind temperatures.

We suggest that our wind models should be modified to increase the emission measure of high-density layers, i.e., increase the amount of "chromospheric" material.

The Na I atom is also easily ionized and is therefore present only in the densest or high mass-loss rate wind models. Na I blueshifted (wind) absorption occurred only in models 6 and 15, which have $\dot{M} = 10^{-7}\ M_\odot\ \mathrm{yr}^{-1}$. Our results are in good agreement with those of Natta and Giovanardi (1990), who have independently constructed an extensive grid of wind models and find little Na I wind absorption below $10^{-7}\ M_\odot\ \mathrm{yr}^{-1}$.

In some cases fairly broad Na I emission is observed in TTS without a strong blueshifted absorption component. Only models 6, 15, and 19 produced Na I resonance line emission. It was necessary to adopt a large turbulent broadening velocity field (50 km s^{-1}) in the "chromosphere" of model 19 in order to reproduce the observed line widths. The line profiles will be discussed in more detail in § IV.

As described in the Appendix, we have constructed a simple one-zone or slab model which indicates the combination of densities and temperatures required to produce Ca II and Na I emission. Figure 9 indicates that Na I emission can be produced at densities $>10^{11}$ cm^{-3} at temperatures in excess of 8000 K. The $\dot{M} = 10^{-7}\ M_\odot\ \mathrm{yr}^{-1}$ models have hydrogen densities $\sim 2 \times 10^{11}$ cm^{-3} at $r \sim 1.5\ R_*$, and for temperatures $T \gtrsim$ 10,000 K, Na I emission results, in agreement with Figure 9. Alternatively, Na I emission may arise in a high-density region of much lower temperature, as in model 19.

We also show similar slab emission calculations for Ca II in Figure 9. At a given temperature, for increasing densities the Ca II K line goes into emission first, followed by the Ca II infrared triplet, followed by Na I emission. Figure 9 indicates that smaller emission measures are required to produce Ca II emission than Na I emission.

Note that Figure 9 does *not* constrain the optical depth in the lines. That is, emission or absorption may be unobservably small at the lowest densities or highest temperatures considered.

d) Wind Radiative Losses; Balmer and Paschen Continuua

For models with the highest mass-loss rates, substantial Balmer and Paschen-continuum emission arises in the wind. In particular, the $10^{-7}\ M_\odot\ \mathrm{yr}^{-1}$, $T \gtrsim 10{,}000$ K wind models (models 6, 15, and 21) exhibit more luminosity in these continuua than from the stellar photosphere (see Fig. 10). In addition, model 15 exhibits a very large Paschen jump, which is not apparent in Kuhi's (1974) observations. Our results reinforce the conclusion that high $\dot{M}$ winds cannot have very high tem-

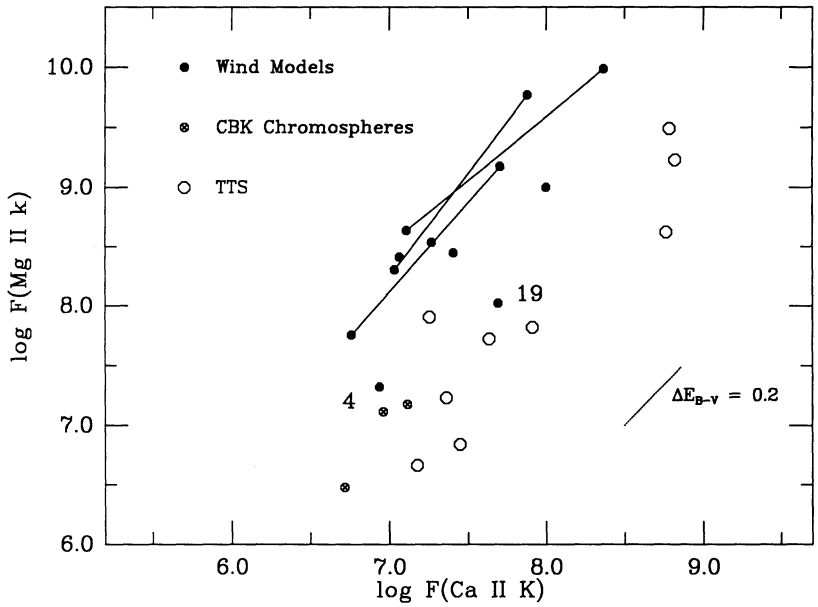

FIG. 8.—Relationship between Ca II K and Mg II *k* line emission. A reddening vector for a change in $E(B-V)$ of 0.2 mag is shown, assuming the standard reddening law.

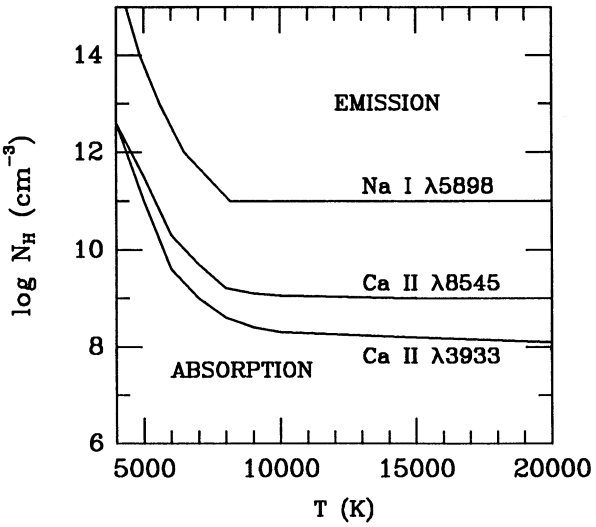

FIG. 9.—Parameters for which Ca II and Na I emission or absorption lines are produced in an isothermal slab of constant density and thickness of one stellar radius. The assumptions used in constructing the schematic dividing lines between emission and absorption regions are discussed in the Appendix.

peratures, as suggested by Natta *et al.* (1988). The reason is that there is not enough mechanical energy available to balance the huge radiative losses of such massive hot (and therefore ionized) winds.

Figure 10 indicates that high mass-loss rate winds with temperatures approaching 10,000 K exhibit Balmer and Paschen continuum emission. Basri and Bertout (1988) developed accretion disk boundary layer models in which optically thin Paschen-continuum radiation arises from the boundary layer. Basri and Bertout argue that such continuua in TTS are necessarily the signature of boundary layer emission. However, we note that massive winds can also produce such emission (the optical depth at 5000 Å in the wind of model 15 is ~0.25). It seems quite possible that some of the hydrogen bound-free emission arises in the wind, particularly since the stars with strongest emission tend to have the blueshifted Na I absorption indicating high mass-loss rates. Distinguishing between wind and boundary layer contributions may not be easy.

Although we constructed several trial model atmospheres, we were unable to construct a model which exhibited Na I emission that did not also have substantial Balmer- and Paschen-continuum emission. Note that the excess Balmer and Paschen continuua are much larger in model 15 than in the chromospheric model (model 19). Simultaneous measurements of optical continuum veiling and Na I emission may help differentiate between Na emission formed in an extended, hot, low-density region or in a dense, high-density, low-temperature layer.

e) Effects of Velocity Fields on Fluxes

In order to examine the sensitivity of our results to the character of the velocity fields, line fluxes for model 12 were calculated using both the moving source function and escape probability methods. As shown in Table 6, the differences are not large. We also calculated the line fluxes for the same temperature and density structure as model 12, but for zero expansion velocity. The results shown in Table 6 indicate little change for Mg II and Ca II. The Hα flux increases by a factor of ~3 in the static case because the line center optical depth in the outer layers increases without the expansion velocity gradient, and the decreased photon escape leads to larger source functions (see Appendix).

Natta, Giovanardi, and Palla (1988) calculated hydrogen line fluxes for isothermal expanding winds with *no* turbulent velocity. A comparison with our results for Hα is shown in Figure 4. The agreement is reasonable, considering that the calculations of Natta, Giovanardi, and Palla (1988) assume a different photospheric temperature (4500 K), a slightly different expansion velocity, a different stellar radius (7 $R_\odot$), and no turbulent broadening velocity.

We conclude that the source functions for the emission lines of H, Mg II, and Ca II are not extremely sensitive to the differing velocity fields considered here. However, the line profiles

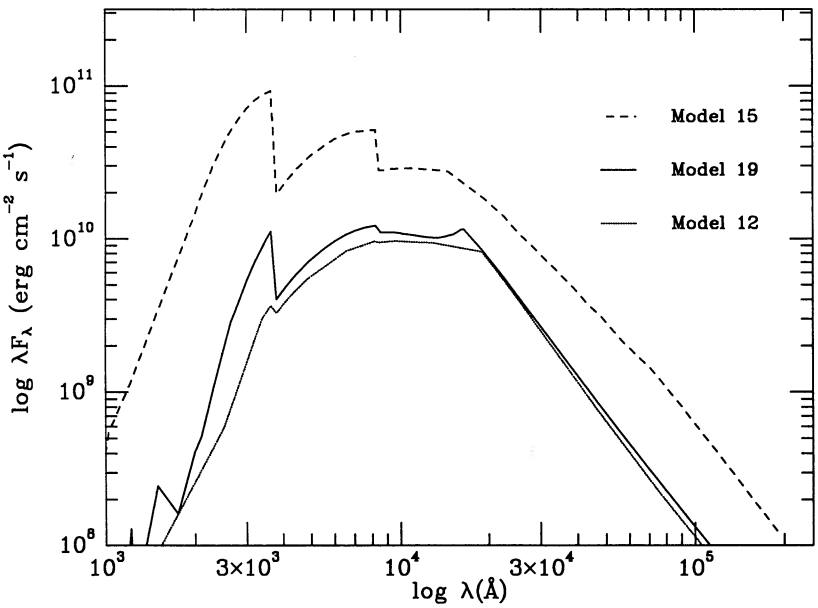

FIG. 10.—Continuum emission from wind models 12, 15, and 19

TABLE 6

COMPARISON OF LINE FLUXES FOR MOVING SOURCE FUNCTION, STATIC, AND ESCAPE PROBABILITY MODELS

Model 12	$F(H\alpha)$	$F(H\beta)$	$F(H\gamma)$	F(Mg II)	F(Ca II)
MSF, 14 lines (H)	5.5E7	7.1E6	2.2E6	...	...
MSF, 7 lines (H)	5.6E7	7.3E6	1.6E6	...	...
MSF (Mg II, Ca II)	...	...	...	3.4E8	1.5E7
Escape probability	5.0E7	6.1E6	1.5E6	2.6E8	1.9E7
Static case	1.4E8	1.7E7	6.3E6	...	...

NOTE.—Surface fluxes F are in units of ergs cm^{-2} s^{-1}. MSF = moving source function calculations with indicated number of transitions explicitly considered; other permitted transitions in the eight-level hydrogen atom are calculated with escape probabilities. All calculations use the model 12 density and temperature structure.

do depend sensitively on the velocity fields, as shown in the following section.

f) *Infrared Line Fluxes*

Model 12 produces luminosities of 1.4×10^{30} ergs s^{-1}, 6.3×10^{29} ergs s^{-1}, and 9.3×10^{29} ergs s^{-1} in Paα, Brα, and Brγ, respectively. Model T4 produces essentially the same fluxes, while the escape probability results for model 15 give fluxes of 1.1×10^{31} ergs s^{-1}, 1.3×10^{30} ergs s^{-1}, and 1.0×10^{31} ergs s^{-1} for the same three lines. In general few observations of infrared hydrogen emission exist for TT stars. Observations of T Tauri (Persson *et al.* 1984; Evans *et al.* 1987) suggest a Brα luminosity of 4×10^{30} ergs s^{-1} to 1×10^{31} ergs s^{-1}. Model 12 scaled to the $\sim 6\ R_\odot$ radius of T Tau would provide $\sim 2.5 \times 10^{30}$ ergs s^{-1}, 2–4 times smaller than that observed, suggesting that T Tauri may have a larger mass loss rate than employed in model 12. The model 12 ratio of Brα/Brγ = 0.7 is substantially smaller than the ratio of 2–3 estimated for T Tauri by Evans *et al.* (1987), but consistent with measurements of DG Tau by the same authors. The isothermal wind calculations of Natta, Giovanardi, and Palla (1988) indicate Brα/Br$\gamma \gtrsim 0.8$; the discrepancy may arise because most of the Br line flux in our models originates in the chromospheric layers, not in the wind.

IV. LINE PROFILES

In this section we exhibit line profiles calculated for several models. We discuss the differences between model profiles and observations only briefly, deferring a more detailed comparison for Paper II, in which we show that the resulting profiles depend sensitively on the assumed geometry of the outflow.

a) *Hydrogen Lines*

We consider the line profiles of models 12 and T4 in greatest detail, since the MRT treatment should provide the most accurate source function calculations. In Figure 11 we show Balmer line profiles for model 12. The basic features of the Balmer line profiles are produced by blueshifted absorption, arising from outer, expanding layers where the line source function declines, superposed on broad emission originating from deep regions with large turbulent motions. The Hα line is still optically thick out to $\sim$2–3 Doppler widths from line center, and the emission arises on the wings of the Gaussian broadening velocity field.[4]

The Hα line has a small amount of blueshifted emission at more negative velocities than the blueshifted absorption. This type of blueshifted emission in Hα is commonly observed in TTS (e.g., Hartmann 1982; Schneeberger *et al.* 1979). The lower optical depths of Hβ and Hγ in the expanding envelope result in lower line source functions, producing strong blueshifted absorption, so that the higher Balmer lines look much more like "normal" P Cygni profiles level.

A general comparison with previously published profiles (Herbig 1962; Kuhi 1964; Herbig 1977; Schneeberger *et al.* 1979; Hartmann 1982; Mundt 1984; Finkenzeller and Basri 1987; Basri *et al.* 1989) suggests some qualitative similarities between the calculated profiles and observations of some stars. However, most observations indicate much more symmetric Hα and Hβ line profiles. Also, the observed absorption reversals in Hα and Hβ tend not to go below the continuum (Ulrich 1976; Basri *et al.* 1989). The blueshifted absorption features also are generally observed to be substantially narrower than exhibited by our calculations in the left-hand panels of Figure 11.

As noted before, the assumption of isotropic line broadening is not consistent with the specific hydrodynamic model used, which assumes propagating transverse Alfvén waves. In order to see the effect of this approximation, we used the same source functions but changed the turbulent broadening velocity to represent entirely tangential wave motions. The right-hand panels of Figure 11 show that the adoption of tangential broadening does not change the emission widths very much for Hα and Hβ, but makes the absorption reversal narrower, in better agreement with observations.

Figure 12 also shows model 12 line profiles predicted for some near-infrared emission lines of interest. Note that the continuua are only those of the underlying photosphere and do not include an infrared-emitting disk (Lynden-Bell and Pringle 1974; Adams, Lada, and Shu 1987; Kenyon and Hartmann 1987). The model 12 Brα line width (FWHM) of $\sim$300 km s^{-1} is a factor of 2 larger than that observed by Persson *et al.* (1984). However, the model 12 Hα line width is larger than observed in T Tau by a similar factor, so that a slower expansion velocity could be employed to explain the observations.

In general the blueshifts of the absorption features in the calculated profiles are about a factor of 2 larger than observations of the optical hydrogen lines. Using the line source functions from model 12, we recomputed line profiles after halving the expansion velocity at each radius. The results are shown in Figure 13. The reduction in expansion velocity results in blueshifted emission for both Hα and Hβ, in better agreement with observations. However, we note that the absorption reversals are still too deep.

[4] We emphasize that the wave motion is assumed to result in Gaussian microturbulent broadening for simplicity, but this may not be correct. The net effect of the Gaussian assumption is to provide wings with velocities several times the mean wave amplitude in very optically thick lines.

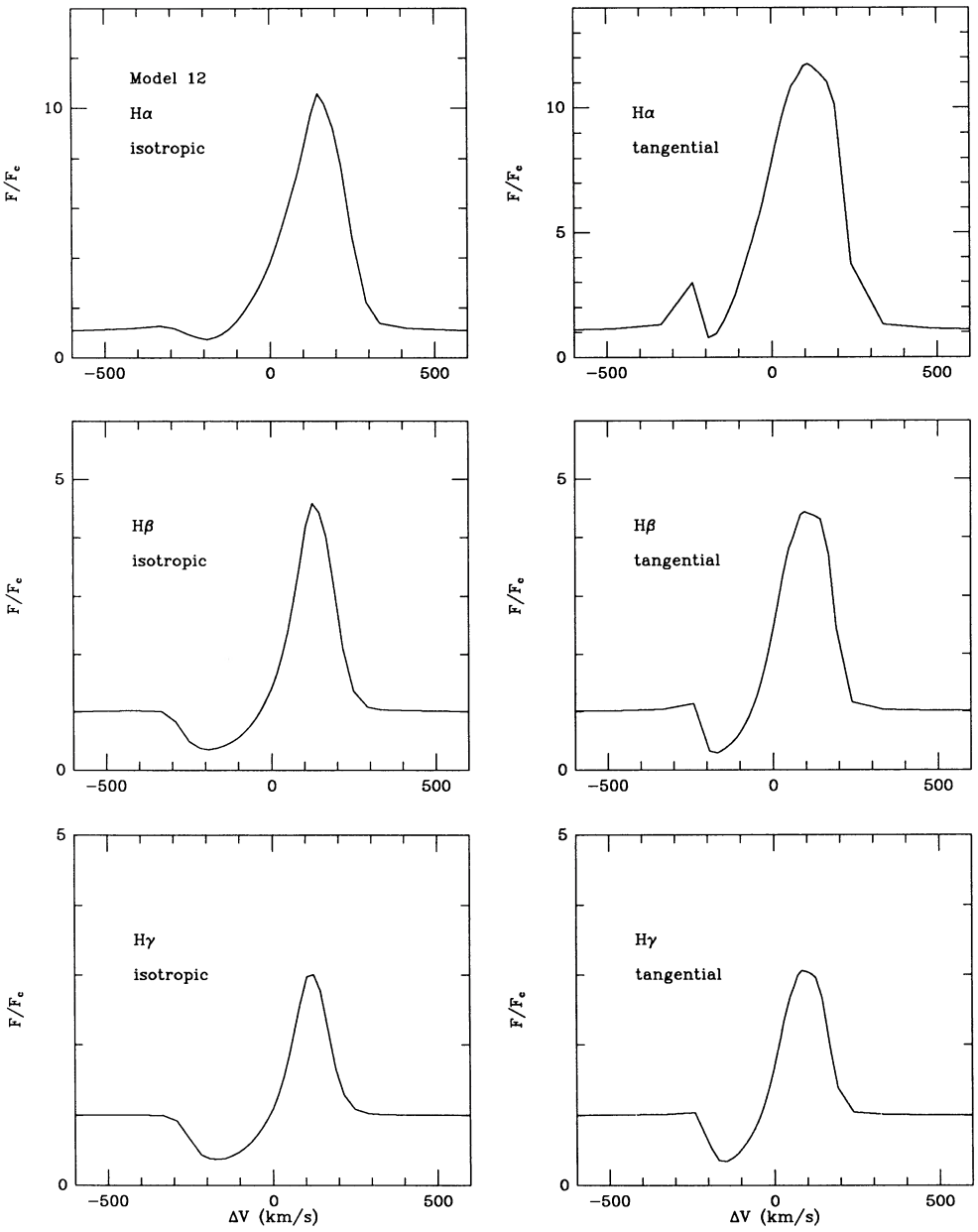

FIG. 11.—Balmer line profiles for wind model 12, constructed using the moving radiative transfer (MRT) method. The left-hand panels are results for assuming that the wave broadening is isotropic. Results in the right-hand panels assume that the supersonic line broadening is everywhere tangential to the radial direction. The effect of the tangential broadening, which more accurately represents propagating Alfvén waves in a radial magnetic field geometry, is to narrow the blueshifted absorption components.

The deep absorption reversal seen in these profiles results from the low values of the line source functions in the expanding envelope. One would expect that the absorption reversals therefore would be less deep in models with higher envelope temperatures. To test this hypothesis, we constructed model T4, which has the same temperature structure as model 1, but a slightly higher mass loss rate of $10^{-8}\ M_\odot\ \mathrm{yr}^{-1}$ in order to make a closer comparison with model 12. As shown in Figure 14, the hydrogen line profiles produced by this model have much higher absorption reversals, as expected. In general, the agreement with observations seems somewhat better for this high-temperature wind model. We hesitate to conclude, however, that $T_{\max} \sim 30{,}000$ K is therefore required by the observations. As we show in Paper II, departures from spherical symmetry in low-temperature winds can also produce apparent "absorption" reversals in better agreement with observations.

Basri and Bertout (1989) argue that the similarity of high Balmer series line profiles, coupled with accretion models for TTS, suggests that the high Balmer series lines come from the boundary layer region. We note that the profiles of the high Balmer lines in our models are all extremely similar, because these lines come from the same region of the wind. High-resolution profiles can constrain outflow velocities in the region of high Balmer line formation.

For comparison we show hydrogen line profiles for the high-

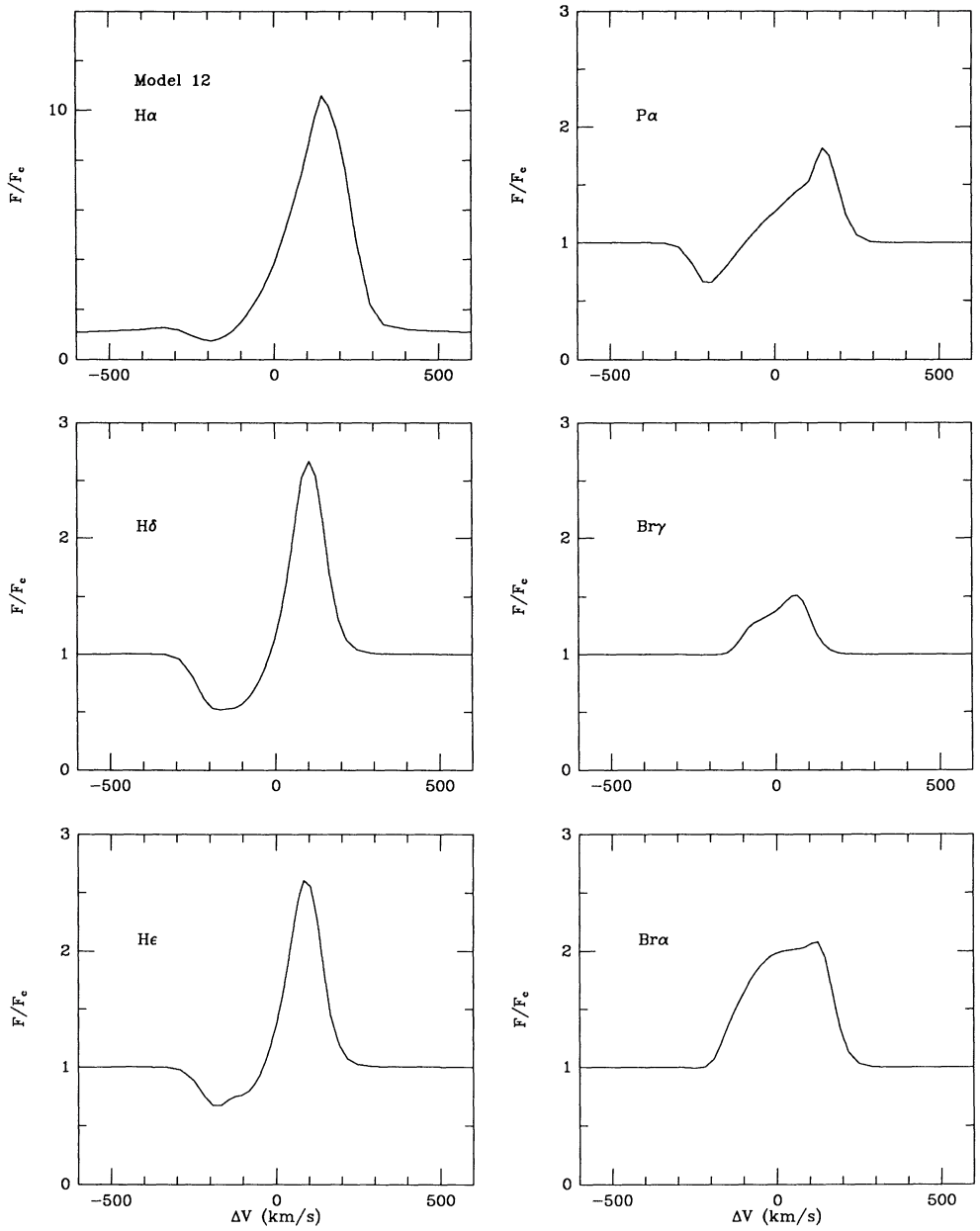

FIG. 12.—Additional hydrogen line profiles for model 12 with isotropic wave broadening

mass loss rate model 15 in Figure 15. The source functions have been calculated using the escape probability approximation, so that details of the profiles should not be taken too seriously.

b) Mg II *k and* Ca II

In Figure 16 we show the line profiles for the Mg II *k* and Ca II K resonance lines for model 12. Partial redistribution effects were taken into account in computing these profiles in the moving atmosphere (see Vernazza, Avrett, and Loeser 1981). Comparison with observed profiles (see Kuhi 1964; Brown, Ferraz, and Jordan 1984; Mundt 1984) suggests that the models exhibit too little blueshifted emission, as in the case of the hydrogen lines. Tangential broadening might produce better agreement with the observed profiles.

A sequence of escape probability profiles for the Ca II resonance and infrared triplet lines is shown in Figure 17. The sensitivity of the resonance line profile to mass-loss rate and wind temperature is evident. We find no Ca II triplet wind emission unless mass-loss rates are extremely high, although some blueshifted absorption may be produced in the lower mass-loss rate winds. Thus, the typical Ca II triplet emission seen in TTS (cf. Basri *et al.* 1989) must be produced in denser "chromospheric" layers than we have adapted here.

c) Na I *Profiles*

We show Na I line profiles for models 19 and 15 in Figure 18. We have not allowed for line overlap in the calculations for model 15, but the neglect should not seriously affect our conclusions. A deep absorption reversal causes the somewhat

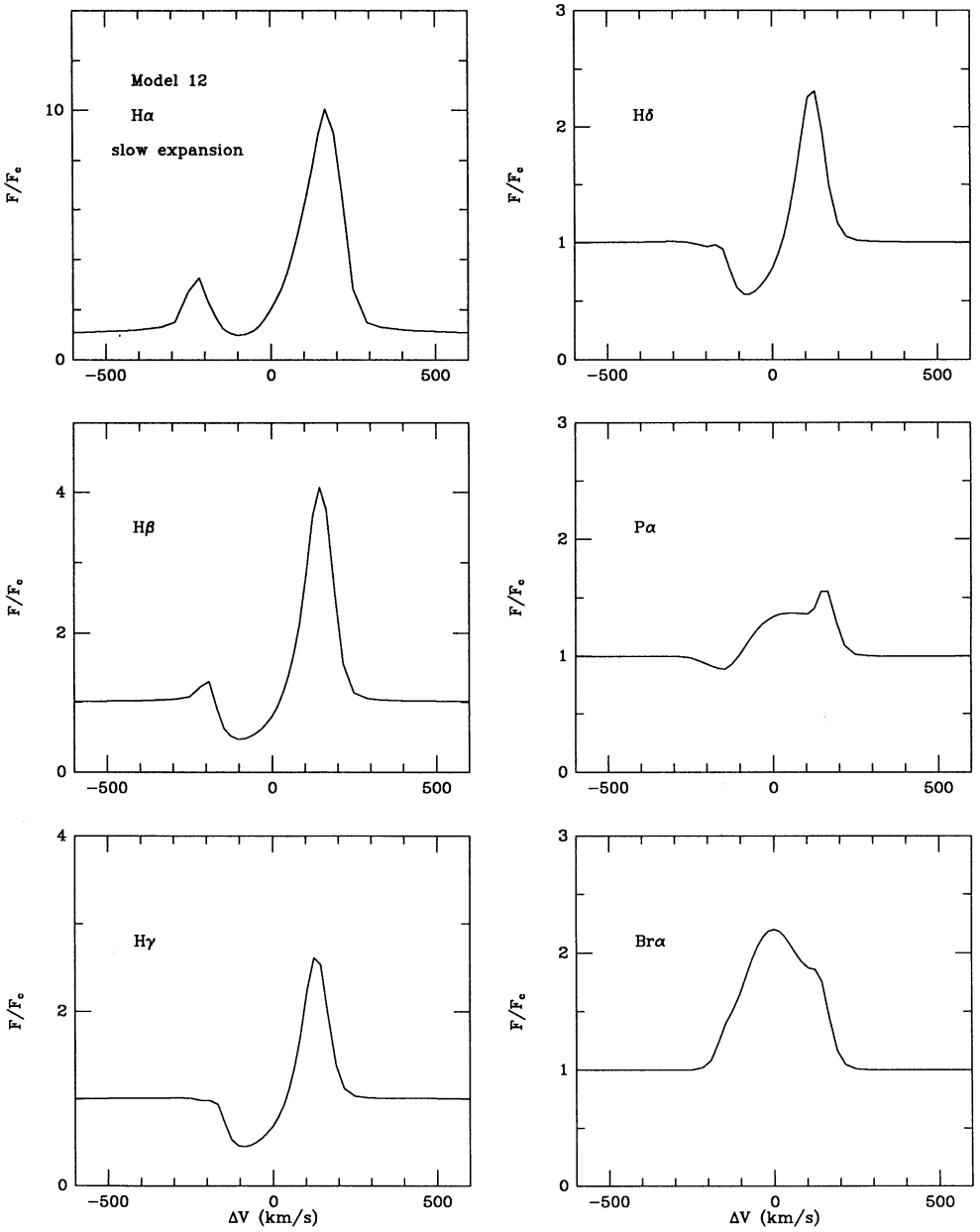

FIG. 13.—Hydrogen line profiles using the same source functions and level populations as in model 12, but with wind velocities decreased by a factor of 2 at all radii.

peculiar appearance of the model 19 profiles, where the emission in the D_1 line appears to be weaker than the D_2 line, an effect that is not apparent in existing observations (Hartmann 1982; Mundt 1984). Model 19 assumes a very large turbulent velocity of 50 km s^{-1} in the very deep chromospheric layers in order to produce Na I emission widths comparable to those observed. Mundt's (1984) observations suggest that in most cases where Na I emission or absorption is noticeable, the profiles are somewhat intermediate in appearance between models 19 and 15, with blueshifted emission extending beyond the blueshifted absorption.

d) Implications for "Turbulence"

In general, the comparison of most of our line profiles with observations would be improved if the expansion velocity were somewhat reduced with respect to the "turbulent" velocity. The presence of the "turbulent" velocity component is absolutely essential to obtaining emission at greater blueshifts than absorption, as observed. In principle one could reduce the blueshifts of the absorption by invoking a decelerating flow, as in Kuan's (1975) models. However, it seems unphysical to start the flow at high velocities, as Kuan did; one must allow for an acceleration region, and so the problem of blue shifted emission will remain for lines formed in the accelerating flow.

V. CONCLUSIONS

The model wind calculations reported in this paper indicate that the Hα emission of TTS originates in extended stellar envelopes with temperatures $\gtrsim 8000$ K, with the higher Balmer lines formed much closer to the star. With the assumed velocity

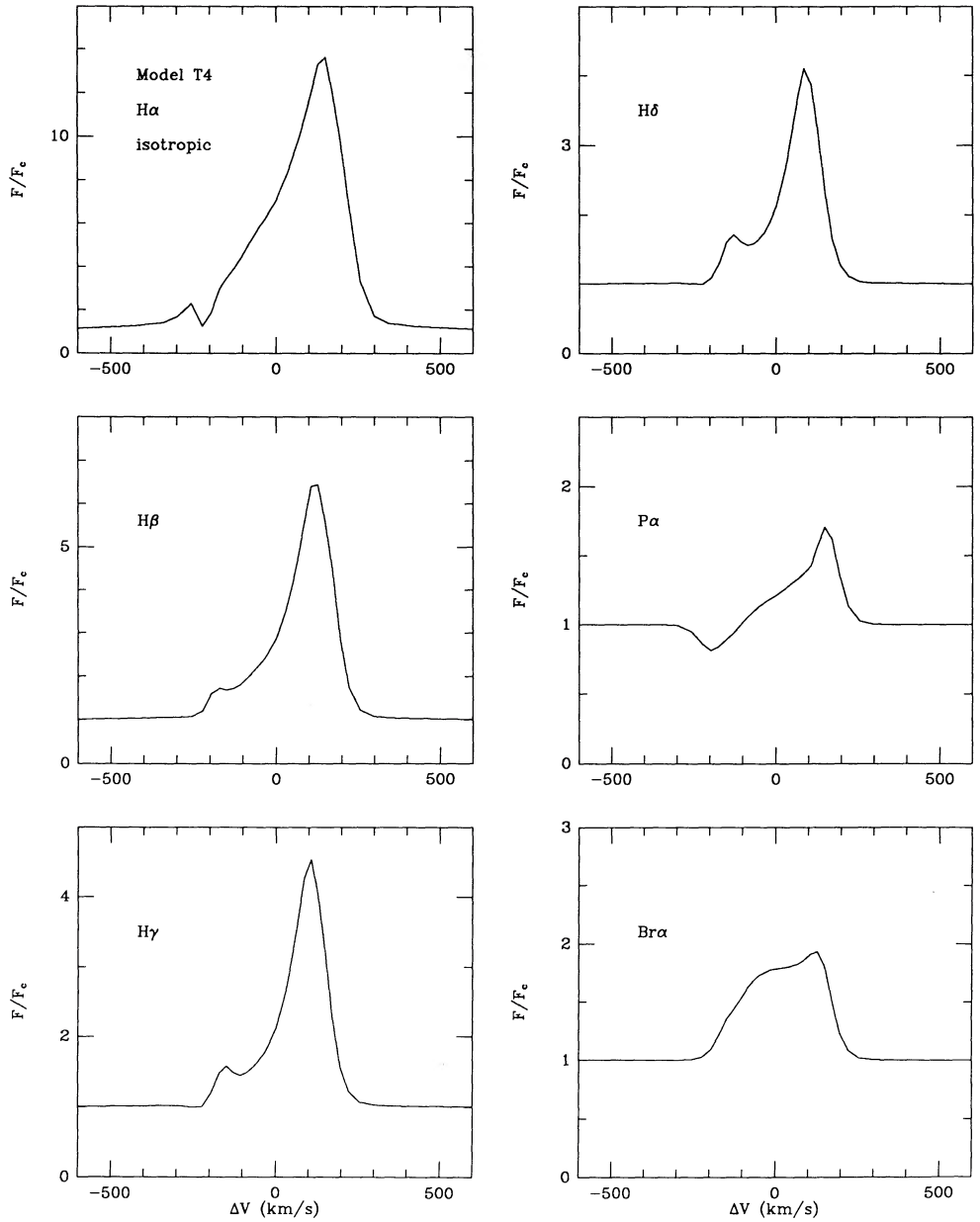

FIG. 14.—Hydrogen line profiles for model T4, in which the maximum wind temperature is $\sim 3 \times 10^4$ K (model 5 of HEA). In this case the higher outer envelope temperatures produce much higher absorption reversals than in model 12 (Fig. 10), in better agreement with observations.

fields, the Hα emission observed indicates a typical mass loss rate of $\sim 10^{-8}\ M_\odot\ \mathrm{yr}^{-1}$, in approximate agreement with results from studies of the broad forbidden lines (Jankovics, Appenzeller, and Krautter 1983; Appenzeller, Jankovics, and Ostreicher 1984; Edwards *et al.* 1987).

The wind models produce larger Mg II resonance line fluxes than observational estimates for some TTS. The observed fluxes are quite sensitive to the adopted extinction, and there is some evidence to indicate that TT reddenings have been systematically underestimated (Hartigan *et al.* 1989; Hartmann and Kenyon 1990). Even modest increases in reddening corrections would produce better agreement between the models and observations. Otherwise, there is some fundamental discrepancy between our models and TT winds, perhaps due to the assumption of homogeneity.

Our calculations, along with the extensive grid of wind models calculated by Natta and Giovanardi (1990), indicate that mass loss rates approaching $10^{-7}\ M_\odot\ \mathrm{yr}^{-1}$ are required to produce blueshifted Na I absorption. Such Na I absorption is rather rare, so that we infer mass-loss rates for most TTS $< 10^{-7}\ M_\odot\ \mathrm{yr}^{-1}$. The models indicate that Na I resonance line emission (as distinct from absorption) is difficult to produce to any substantial degree without simultaneously producing substantial Balmer-continuum emission. Our results suggest that the Na I emission can be used to constrain velocity fields and densities in the regions where the hydrogen bound-free excess emission of TTS arises. Simultaneous observations of the Balmer jump and Na I profiles may help distinguish between the competing chromospheric and boundary layer models for the excess continuum emission in TTS.

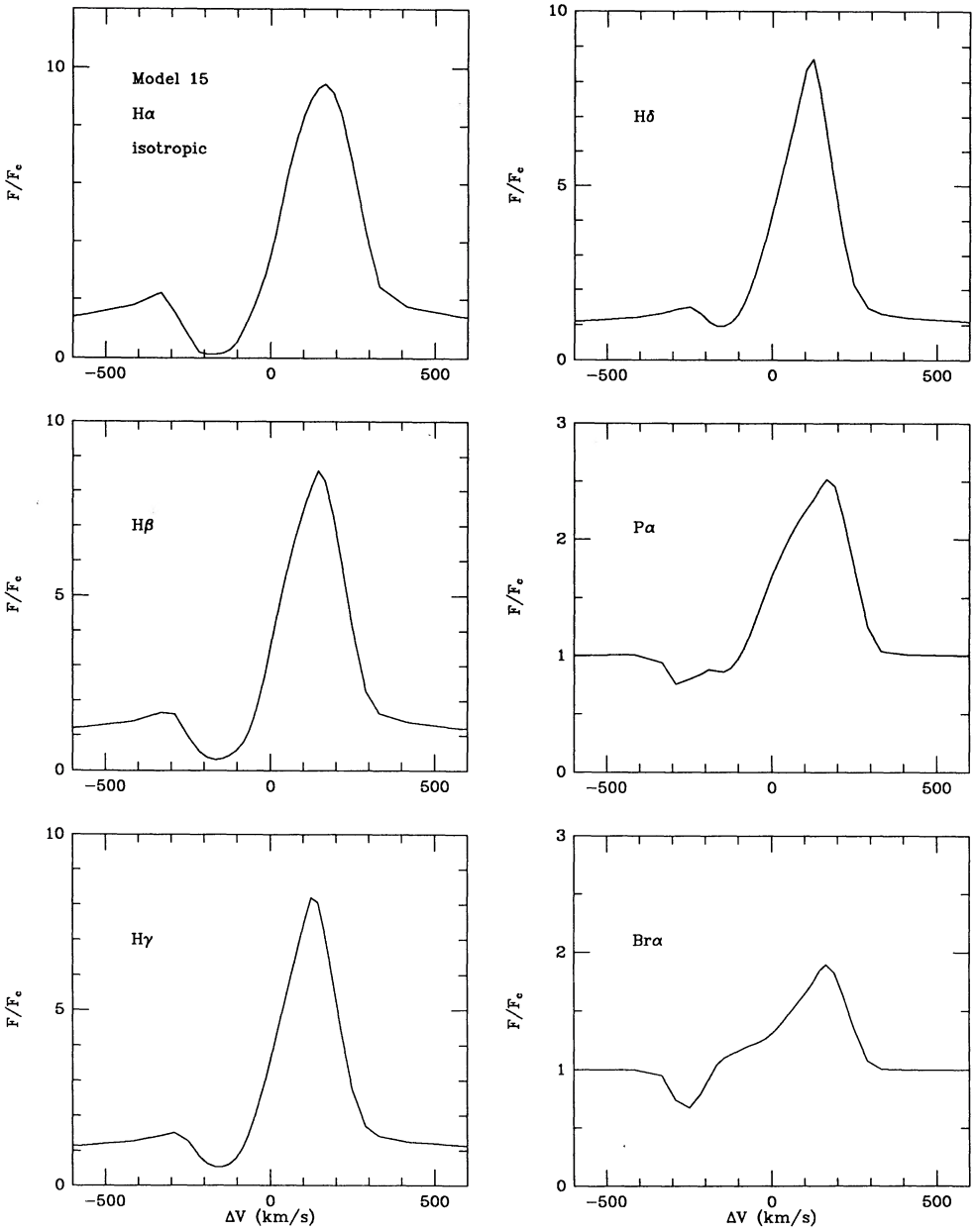

FIG. 15.—Hydrogen line profiles for model 15, calculated using escape probability methods

We find rather deep absorption reversals in the hydrogen lines for a wind model in which the gas temperature does not rise beyond $\sim 1 \times 10^4$ K. These absorption reversals are far deeper than normally observed. This problem can be alleviated if the wind temperature continues to rise sufficiently rapidly in the acceleration region, to temperatures $\gtrsim 30{,}000$ K. Alternatively, departures from spherical symmetry may be important (Paper II).

The wind models suggest that large "turbulent" velocities are required to reproduce the observed type III line profiles. These turbulent velocities broaden the emission wings formed at the base of the wind, producing emission at larger blueshifts than the absorption reversal, which is formed further out in the flow. If anything, our models overestimate the expansion relative to the turbulent broadening by a factor of 2 or so. Although we treat the turbulence as a microturbulence for simplicity in the radiative transfer modeling, the observations do not clearly constrain the nature of this turbulence, and this is an additional source of uncertainty in applying our models to observations.

We have not explicitly considered the effects of circumstellar disks in this paper, although there is increasing evidence that TT activity results from disk accretion (Lynden-Bell and Pringle 1974; Kenyon and Hartmann 1987; Bertout, Basri, and Bouvier 1988; Basri and Bertout 1989). The large velocities in the inner disk (Keplerian velocities ~ 200 km s^{-1}) provide an attractive source for the "turbulent" motions required to explain the line profiles, and an energy source

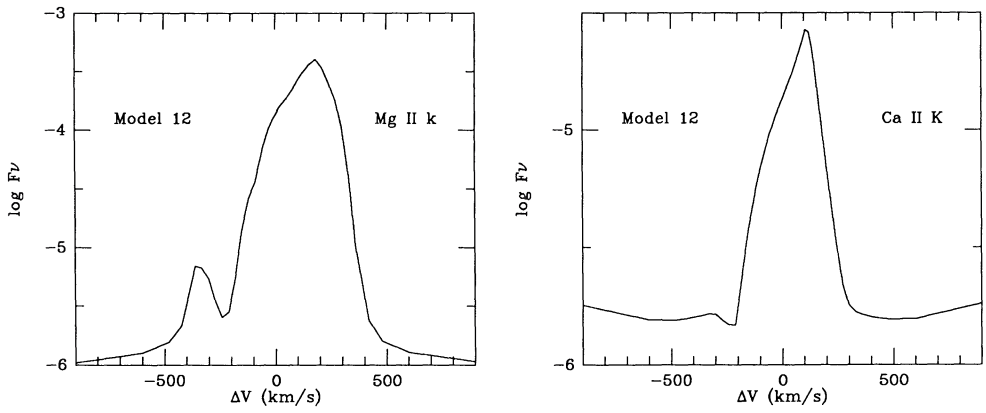

FIG. 16*a* FIG. 16*b*

FIG. 16.—(*a*) Mg II *k* and (*b*) Ca II K line profiles for model 12, calculated with partial redistribution for moving atmospheres

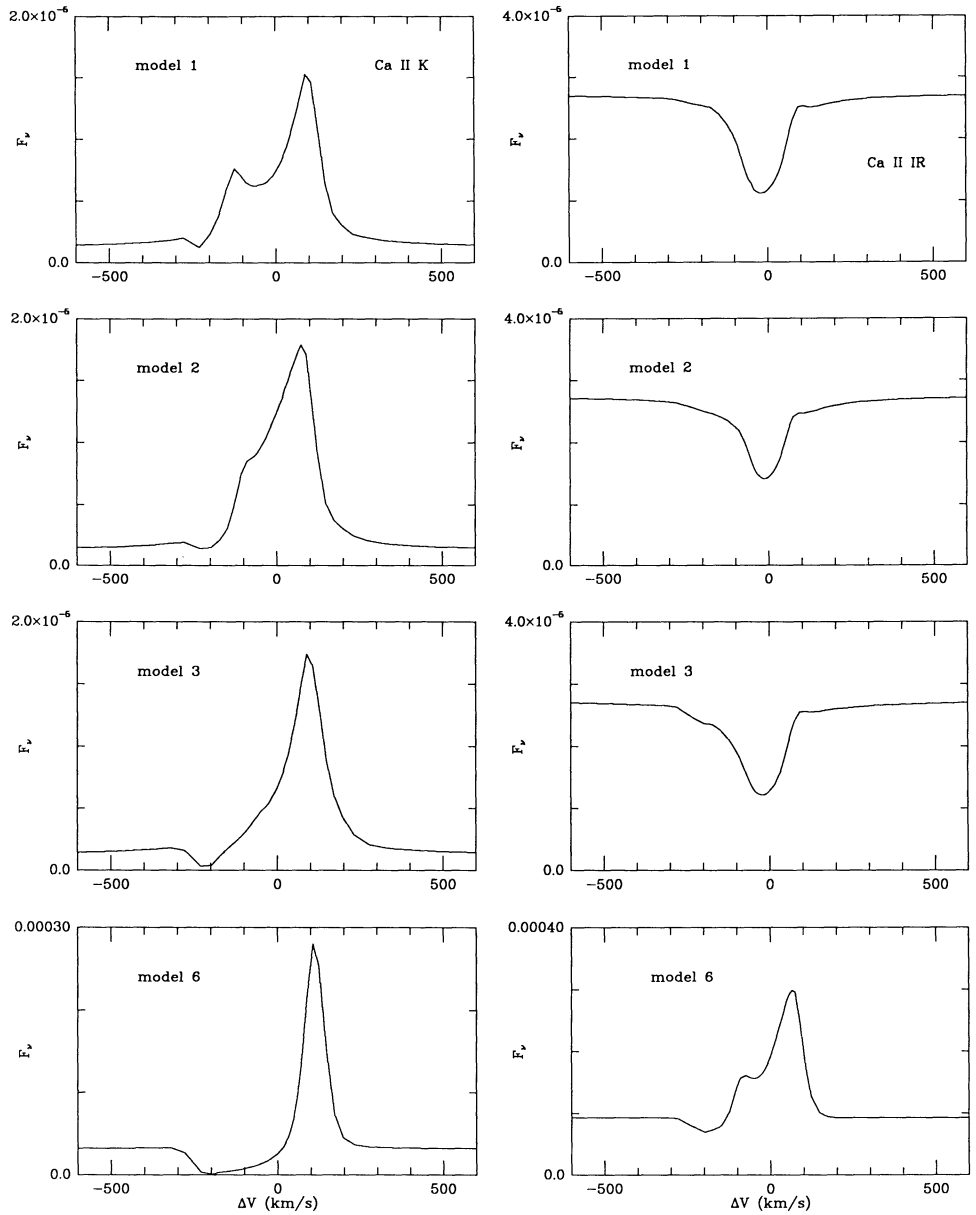

FIG. 17.—Ca II resonance line and infrared triplet profiles for a series of models calculated using escape probabilities

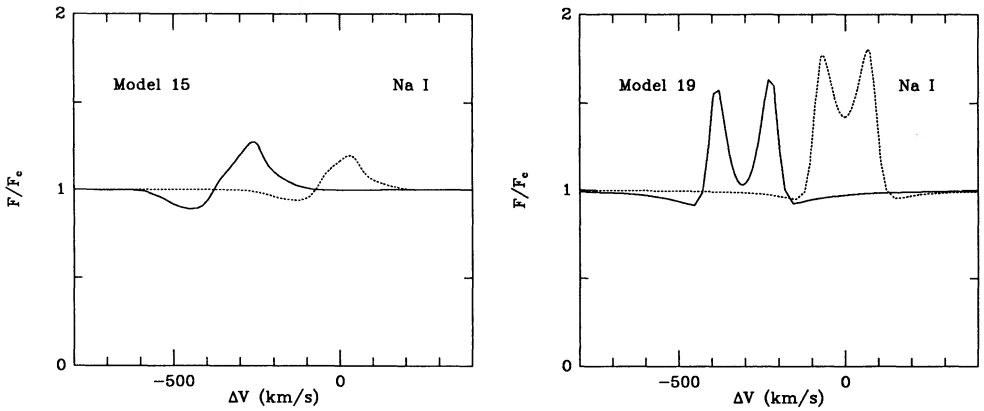

FIG. 18*a* FIG. 18*b*

FIG. 18.—(*a*) Na I resonance line profiles for model 15. (*b*) Na I resonance line profiles for model 19.

which can potentially drive outflow (Blandford and Payne 1982; Pringle 1989), although detailed hydrodynamical calculations have not yet been performed for T Tauri stars. Winds from the disk or boundary layer are not likely to be spherically symmetric; in Paper II we examine the effects of nonspherical wind geometry on line profiles.

We acknowledge useful discussions with Antonella Natta concerning Na I calculations prior to publication and thank Gibor Basri for providing observed line profiles for our inspection. This work was supported by NASA grant NAGW 511 and by the International Exchange Program of the Smithsonian Institution.

APPENDIX

LINE SOURCE FUNCTION BEHAVIOUR

The behavior of line fluxes in the wind models can be understood in terms of the line source functions, which in turn depend upon the ratio of upper to lower populations n_u/n_l. We have derived expressions from the detailed results of the Pandora code (Avrett and Loeser 1984) which reproduce population ratios within factors of ~ 2 in the regions of interest. For hydrogen, the population ratios for the lower levels can be written as

$$\frac{n_2}{n_1} = \left(\frac{n_2}{n_1}\right)^* \frac{C_{21}}{C_{21} + A_{21}\rho_{21}} \tag{A1}$$

and

$$\frac{n_3}{n_1} = \left(\frac{n_3}{n_1}\right)^* \frac{(n_\kappa/n_1)(n_1/n_\kappa)^* R_{\kappa 3} + C_{31} + (n_2/n_1)(n_1/n_2)^* C_{32}}{C_{31} + C_{32} + A_{31}\rho_{31} + A_{32}\rho_{32} + R_{3\kappa}}, \tag{A2}$$

where we have identified the net radiative bracket with the escape probability ρ. Here starred quantities refer to LTE values; the C_{ij} are collision rates from level i to level j, A_{ij} are the Einstein spontaneous emission rates, and $R_{i\kappa}$ and $R_{\kappa i}$ are the bound-free radiative rates to and from the continuum, respectively.

Since the optical depth in Lyman-α is large and $\rho \propto 1/\tau$, the ratio of populations in the first two levels of hydrogen is close to LTE values throughout most of the envelope. Thus, Lyman-α is thermalized except in the outermost regions. In contrast, the ratio n_3/n_1 is generally far from thermalization. We distinguish three regions of the envelope, where different terms dominate the population ratio in equation (A2):

Region I.—$3 < r < 11\ R_*$:

$$\frac{n_3}{n_1} \approx \left(\frac{n_3}{n_1}\right)^* \frac{(1/b_1)R_{\kappa 3}}{A_{32}\rho_{32} + A_{31}\rho_{31}}, \tag{A3}$$

Region II.—$1.4 < r < 3$:

$$\frac{n_3}{n_1} \approx \left(\frac{n_3}{n_1}\right)^* \frac{C_{31} + C_{32}}{A_{32}\rho_{32}}, \tag{A4}$$

Region III.—$1.0005 < r < 1.4$:

$$\frac{n_3}{n_1} \approx \left(\frac{n_3}{n_1}\right)^* \frac{C_{31} + C_{32} + (1/b_1)R_{\kappa 3}}{A_{32}\rho_{32} + C_{31} + C_{32} + R_{3\kappa}}. \tag{A5}$$

The exact radial regions indicated correspond to model 12 but are generally applicable to all the models. In region I, photon escape dominates, driving down the ratio of populations n_3/n_1. In the higher density region II, collisions become important and the population ratio increases, approaching the LTE value. However, the escape term $A_{32}\rho_{32}$, which is important even in region III, reflecting the fact that photons are escaping through the wings of Hα, prevents the ratio from reaching the LTE value. At the temperature minimum region, for $r < 1.0005\ R_*$, the escape term and the collisional terms become negligible, and the population ratio is determined by the ratio of the continuum rates. The ratio n_3/n_1 does not reach the LTE value until photospheric levels, where the Paschen continuum thermalizes.

The approach to thermalization of the source function, which is approximately proportional to n_3/n_2, depends on the term n_3/n_1, since Lyman-α is thermalized in most of the envelope. As shown in Figure 19*a* for representative models, the outermost regions of the envelope correspond to region I, where escape dominates and the line source function S_ν is low. As density increases and collisions become important, S_ν increases (region II) but does not thermalize due to the importance of the escape term. Nor is S_ν thermalized in the temperature minimum region, where its value is fixed by the ratio of the continuum rates. The source function for all models exhibit the same qualitative behavior, but the position and extent of regions I, II, and III depend upon the density and temperature structure of the model. For the high-density models, the transition to the region where collisions drive the source function to its maximum value (region II) occurs at larger radii than in the lower density models, resulting in higher fluxes because of the increased emitting area. Higher temperatures in the envelope increase collision rates, increasing the source function and the resulting line fluxes.

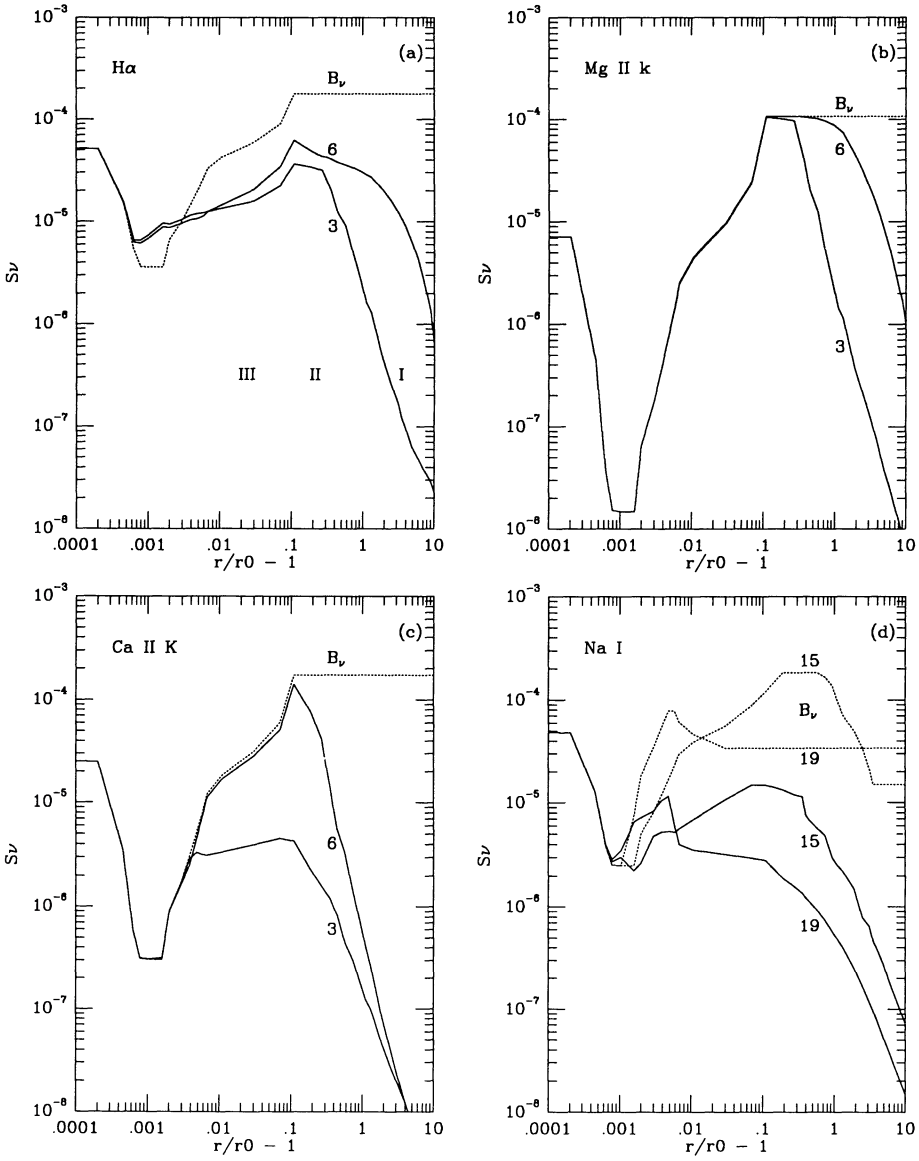

FIG. 19.—Typical line source function distributions for Hα, Mg II *k*, Ca II K, and Na I. Numbers refer to wind models (see Table 1 and Fig. 2), and roman numerals denote regions as described in the Appendix.

From equations (A1) and (A2) we see that the population ratio can generally be described as

$$\frac{n_u}{n_l} = \left(\frac{n_u}{n_l}\right)^* \frac{\text{(collisional terms + continuum terms)}}{\text{(collisional terms + escape terms + continuum terms)}} . \tag{A6}$$

If the optical depth is small, the escape probability will be large and escape terms dominate, resulting in low values for the source function. On the other hand, if the density or the temperature is high, the collisional terms are important and the ratio of populations gets closer to its LTD value.

In the case of Hβ or higher Balmer lines, the line opacity in the envelope is lower than that of Hα, and so the escape probability is larger. Consequently, the source function in the envelope for these lines is lower than that of Hα. Most of the emission in these cases comes from the dense regions close to the star. For the low-density, low-temperature models, Hβ appears in absorption because collisional rates are not sufficient to increase significantly the source function in the envelope, so that the contribution to the flux from this region is too small for the line to be in emission.

In the case of the chromospheric model 19, the contribution from the low-temperature envelope to both Hα and Hβ is small. The source functions for these lines are high only in the high-density, hot inner regions above the temperature minimum, so most of the emission flux comes from the chromospheric region in this model.

Since the energy levels involved in the Mg II k resonance line are far from the continuum, an expression similar to that for Lyman-α (eq. [A1]) provides a good approximation to the results from the detailed Pandora radiative transfer calculations. The line center optical depth in Mg II k is of order 10^3 in the envelope, so that the escape probability is small. The source function in the line thermalizes in the envelope, as shown in Figure 19*b*. Thermalization occurs higher in the envelope the higher the density and/or the temperature of the envelope.

For the resonance line of Ca II K, on the other hand, the optical depth is much lower in the envelope than that of Mg II k, due to the lower abundance of Ca relative to Mg, and to the lower ionization potential of Ca II relative to Mg II. Unlike Mg II, Ca II is ionized in most of the envelope for temperatures greater than $\sim$6000 K, so that the escape probability is large and the source function is low except in high-density, high-temperature regions. Source functions for the Ca II K line are shown in Figure 19*c*. For the low-density wind model 3, the line source function thermalizes just above the temperature minimum, while thermalization occurs at larger radii in the envelope for the high wind density model 6, as expected. Thus, the resonance line flux for the low wind density models depends on the temperature and the density of the region closest to the star, so that among the low-density models the largest Ca II K line emission occurs in the models with denser chromospheres (compare models 1 and 9 in Table 1).

Ca II can be approximated by a three-level atom, neglecting interactions with the continuum. In this case, the ratio of populations can be written as

$$\frac{n_3}{n_1} = \left(\frac{n_3}{n_1}\right)^* \frac{(1 + C_{23}/C_{21})C_{31} + C_{32}}{(1 + C_{23}/C_{21})C_{31} + C_{32} + (1 + C_{23}/C_{21})A_{31}\rho_{31} + A_{32}\rho_{32}} \tag{A7}$$

and

$$\frac{n_3}{n_2} = \left(\frac{n_3}{n_2}\right)^* \frac{(1 + C_{23}/C_{21})C_{31} + C_{32}}{(1 + C_{23}/C_{21})C_{31} + C_{32} + A_{31}\rho_{31} + (1 + C_{13}/C_{12})A_{32}\rho_{32}} . \tag{A8}$$

It is apparent from these equations that lines arising from the transitions between levels 3 and 1 (Ca II H and K) and between levels 3 and 2 (the infrared triplet) do not thermalize as long as the optical depths are small and the escape probabilities high. A slightly higher density is required for n_3/n_2 to reach its LTE value than for n_3/n_1, because of the term $(1 + C_{13}/C_{12})$ multiplying $A_{32}\rho_{32}$ in n_3/n_2, but the difference is not large, so thermalization occurs at similar depths for both lines.

In the grid of models used in this work the infrared triplet of Ca II, represented by the λ8545 line, appears in absorption in all but the high-density models and the chromospheric model. Lines of the triplet and the K line thermalize for the same conditions. However, the continuum at 8545 Å is significantly higher than that at 3933 Å, so a higher flux in the line is required for emission in the infrared triplet to become apparent.

Using expressions (A7) and (A8), we have calculated the flux resulting from a static slab of thickness L, and constant density and temperature n_H and T, A microturbulence velocity Δv is included and the lines are supposed to have Voigt profiles, so that the escape probabilities are calculated with the approximate expressions (Mihalas 1978)

$$P_{esc} = \left(\frac{a}{\pi\tau}\right)^{1/2} , \tag{A9}$$

where a is the damping constant and τ is the total optical depth. The flux at line center F_0 is given by S_ν [1 − exp (− $\tau/\pi^{1/2}$)], and the continuum flux F_{cont} is taken to be the Planck function at the stellar effective temperature. The slab is assumed to be optically thin in the continuum.

In Figure 9 the curves labeled Ca II λ3933 and λ8545 indicate the values of slab temperature and density for which the line center flux F_0 equals the continuum flux F_{cont}. For a given temperature, higher densities produce line emission. The slab model indicates that the Ca II K line turns into emission before the Ca II triplet does, as expected. The results from the simple slab model indicate that Ca II triplet emission can be produced either from the envelopes of high-temperature, high mass-loss rate models or from a denser region, the chromosphere, in the cooler models, in agreement with the detailed calculations.

The Na I atom can be approximated as a three-level atom plus continuum, with $n_3/n_2 = (n_3/n_2)^*$. This approximation reproduces level populations from the detailed calculations to within a factor of 2 in regions of interest. In this case

$$\frac{n_2}{n_1} = \left(\frac{n_2}{n_1}\right)^* \frac{C_{21} + (1/b_1)R_{\kappa 2}}{C_{21} + A_{21}\rho_{21} + R_{2\kappa}} . \quad \text{(A10)}$$

The ionization potential of Na I is 5 eV, so Na II is the dominant state of ionization in the envelope. As a result, the optical depth in the resonance line is small, the escape probability is high, and the line source function is low, except in the highest density regions. The line appears in emission in the high mass-loss rate model 15, and in the chromospheric model 19. Line source functions for model 15 and model 19 are shown in Figure 19*d*. Although the source functions never thermalize in the envelope, due to interactions with the continuum, they increase enough in the envelope, in model 15, or in the chromosphere, in model 19, for the line to be in emission.

We calculated the flux produced by the Na I D_1 line in a manner similar to that used for the Ca II resonance lines, assuming a static slab of thickness L, density n_H, temperature T, and microturbulence Δv, deriving the source function from equation (A10). After substituting the particle conservation equation in equation (A10), we solve this equation and the ionization equation for Na I self-consistently. Radiation temperatures for the continuum have been taken to be 4500 K, and a ν^{-3} dependence has been assumed for the continuum rates. Escape probabilities are given by expression (A9). Line center and continuum fluxes have been calculated as for Ca II. As shown in Figure 9, the threshold density at which the Na I resonance lines turn into emission is higher than that of the Ca II lines at a given temperature, due to the lower optical depths of the Na I lines. At high temperatures, hydrogen densities above 10^{11} are required to have the line in emission, which agrees with the fact that emission from the envelope appears in models with high mass-loss rates. At low temperatures, densities closer to photospheric densities are necessary to produce Na I emission, in agreement with the emission produced by chromospheric model 19, and consistent with the absence of emission in the high mass-loss rate, low-temperature model 8.

REFERENCES

Adams, F. C., Lada, C. J., and Shu, F. H. 1987, *Ap. J.*, **312**, 788.
Appenzeller, I., Jankovics, I., and Ostreicher, R. 1984, *Astr. Ap.*, **141**, 108.
Avrett, E. H., and Loeser, R. 1984, in *Methods in Radiative Transfer*, ed. W. Kalkofen (Cambridge: Cambridge University Press), p. 341.
———. 1987, in *Numerical Radiative Transfer*, ed. W. Kalkofen (Cambridge: Cambridge University Press), p. 135.
Basri, G., and Bertout, C. 1989, *Ap. J.*, **341**, 340.
Basri, B., Rumph, T. F., Batalha, C. C., and Stout, N. M. 1989, *Bull. AAS*, **20**, 1034.
Bertout, C. 1987, in *IAU Symposium 122, Interstellar Matter*, ed. I. Appenzeller and C. Jordan (Dordrecht: Reidel), p. 23.
Bertout, C., Basri, G., and Bouvier, J. 1988, *Ap. J.*, **330**, 350.
Blandford, R. D., and Payne, D. G. 1982, *M.N.R.A.S.*, **199**, 883.
Bouvier, J., Bertout, C., Benz, W., and Mayor, M. 1986, *Astr. Ap.*, **165**, 110.
Brown, A., Ferraz, M. C. de M., and Jordan, C. 1984, *M.N.R.A.S.*, **207**, 831.
Calvet, N., and Albarrán, J. 1984, *Rev. Mexicana Astr. Ap.*, **9**, 35.
Calvet, N., Basri, G., Imhoff, C. L., and Giampapa, M. S. 1985, *Ap. J.*, **293**, 575.
Calvet, N., Basri, G., and Kuhi, L. V. 1984, *Ap. J.*, **277**, 725 (CBK).
Calvet, N., Cantó, J., and Rodríguez, L. F. 1983, *Ap. J.*, **268**, 739.
Calvet, N., and Hartmann, L. 1990, in preparation (Paper II).
Castor, J. 1970, *M.N.R.A.S.*, **149**, 111.
Cohen, M., and Kuhi, L. V. 1979, *Ap. J. Suppl.*, **41**, 743.
Cram, L. E. 1979, *Ap. J.*, **234**, 949.
Cram, L. E., Giampapa, M. S., and Imhoff, C. L. 1980, *Ap. J.*, **238**, 905.
Croswell, K., Hartmann, L., and Avrett, E. H. 1987, *Ap. J.*, **312**, 227.
DeCampli, W. M. 1981, *Ap. J.*, **244**, 124.
Edwards, S., Cabrit, S., Strom, S. E., Heyer, I., and Strom, K. M. 1987, *Ap. J.*, **321**, 473.
Edwards, S., and Snell, R. L. 1982, *Ap. J.*, **261**, 151.
Evans, N. J., II, Levreault, R. M., Beckwith, S., and Skrutskie, M. 1987, *Ap. J.*, **320**, 364.
Feigelson, E. D., and DeCampli, W. M. 1981, *Ap. J. (Letters)*, **243**, L89.
Finkenzeller, U., and Basri, G. 1987, *Ap. J.*, **318**, 823.
Gahm, G. F. 1980, *Ap. J. (Letters)*, **242**, L163.
Hartigan, P., Hartmann, L., Kenyon, S., Hewett, R., and Stauffer, J. 1989, *Ap. J. Suppl.*, **70**, 899.
Hartmann, L. 1982, *Ap. J. Suppl.*, **48**, 109.
———. 1986, *Fund. Cosmic Phys.*, **11**, 279.
Hartmann, L., Edwards, S., and Avrett, E. H. 1982, *Ap. J.*, **261**, 279 (HEA).
Hartmann, L., Hewett, R., Stahler, S., and Mathieu, R. D. 1986, *Ap. J.*, **309**, 275.
Hartmann, L., and Kenyon, S. 1990, *Ap. J.*, **349**, 190.
Hartmann, L., and MacGregor, K. B. 1982, *Ap. J.*, **259**, 180.
Hartmann, L., and Stauffer, J. R. 1989, *A.J.*, **97**, 873.
Herbig, G. H. 1962, *Adv. Astr. Ap.*, **1**, 47.
———. 1977, *Ap. J.*, **214**, 747.
Imhoff, C. L., and Giampapa, M. S. 1980, *Ap. J. (Letters)*, **239**, L115.
Jankovics, I., Appenzeller, I., and Krautter, J. 1983, *Pub. A.S.P.*, **95**, 883.
Jefferies, J. T., and Thomas, R. N. 1959, *Ap. J.*, **129**, 401.
Kenyon, S. J., and Hartmann, L. 1987, *Ap. J.*, **323**, 714.
Krolik, J. H., and Smith, H. A. 1981, *Ap. J.*, **249**, 628.
Kuan, P. 1975, *Ap. J.*, **202**, 425.
Kuhi, L. V. 1964, *Ap. J.*, **140**, 1409.
———. 1974, *Astr. Ap. Suppl.*, **15**, 47.
Kutner, M. L., Leung, C. M., Machnik, and Mead, K. N. 1982, *Ap. J. (Letters)*, **259**, L35.
Lada, C. J. 1985, *Ann. Rev. Astr. Ap.*, **23**, 267.
Lago, M. T. V. T. 1979, Ph.D. thesis, University of Sussex, Brighton.
———. 1984, *M.N.R.A.S.*, **210**, 323.
Lynden-Bell, D., and Pringle, J. E. 1974, *M.N.R.A.S.*, **168**, 603.
Mundt, R. 1984, *Ap. J.*, **280**, 749.
Natta, A., and Giovanardi, C. 1990, in preparation.
Natta, A., Giovanardi, C., and Palla, F. 1988, *Ap. J.*, **332**, 921.
Natta, A., Giovanardi, C., Palla, F., and Evans, N. J., II. 1988, *Ap. J.*, **327**, 819.
Norman, C., and Silk, J. 1980, *Ap. J.*, **238**, 158.
Persson, S. E., Geballe, T. R., McGregor, P. J., Edwards, S., and Lonsdale, C. J. 1984, *Ap. J.*, **286**, 289.
Pringle, J. E. 1989, *M.N.R.A.S.*, **236**, 107.
Pudritz, R. E., and Norman, C. A. 1983, *Ap. J.*, **274**, 677.
Schneeberger, T. J., Worden, S. P., and Wilkerson, M. S. 1979, *Ap. J. Suppl.*, **41**, 369.
Shine, R. A. 1973, Ph.D. thesis, University of Colorado.
Shu, F. H., Lizano, S., Ruden, S. P., and Najita, J. 1988, *Ap. J. (Letters)*, **328**, L19.
Shu, F. H., and Terebey, S. 1984, in *Cool Stars, Stellar Systems, and the Sun*, ed. S. Baliunas and L. Hartmann (Berlin: Springer), p. 78.
Simon, M., Felli, M., Cassar, L., Fischer, J., and Massi, M. 1983, *Ap. J.*, **266**, 623.
Strom, K. M., Strom, S. E., Kenyon, S. J., and Hartmann, L. 1988, *A.J.*, **95**, 534.
Ulrich, R. K. 1976, *Ap. J.*, **210**, 377.
Vernazza, J. E., Avrett, E. H., and Loeser, R. 1981, *Ap. J. Suppl.*, **45**, 635.
Vogel, S. N., and Kuhi, L. V. 1981, *Ap. J.*, **245**, 960.

EUGENE H. AVRETT, LEE HARTMANN, and RUDOLF K. LOESER: Center for Astrophysics, 60 Garden Street, Cambridge, MA 02138

NURIA CALVET: Centro de Investigaciones de Astronomia, Apartado 264, Mérida 5101-A, Venezuela